

Modeling Lunar Pyroclasts to Probe the Volatile Content of the Lunar Interior

Darien Florez¹, Christian Huber¹, Ralph E. Milliken¹, and Julia Berkson¹

¹Brown University

November 26, 2022

Abstract

Constraining the volatile budget of the lunar interior has important ramifications for models of Moon formation. While many early and previous measurements of samples acquired from the Luna and Apollo missions suggested the lunar interior is depleted in highly volatile elements like H, a number of high-precision analytical studies over the past decade have argued that it may be more enriched in water than previously thought. Here, we integrate recent remotely sensed near-infrared reflectance measurements of several Dark-Mantle-Deposits (DMDs), interpreted to represent pyroclastic deposits, and physics-based eruption models to better constrain the pre-eruptive water content of lunar volcanic glasses. We model the trajectory and water loss of pyroclasts from eruption to deposition, coupling eruption dynamics with a volatile diffusion model for each pyroclast. Modeled pyroclast sizes and final water contents are then used to predict spectral reflectance properties for comparison with the observed orbital near-infrared data. We develop an inversion scheme based on the Markov-Chain Monte-Carlo (MCMC) method to retrieve constraints between governing parameters such as the initial volatile content of the melt and the pyroclast size distribution (which influences the remotely measured water absorption strengths). The MCMC inversion allows us to estimate the primordial (pre-eruption) water content for different DMDs and test whether their source is volatile-rich. Our results suggest that the parts of the lunar interior sampled by the source material of the DMDs investigated in this study range in water content from 400 to 800 ppm.

Supplements

Water loss calculations:

In order to use water and grain size dependent remote sensing data (ESPAT) transects on DMDs to investigate the presence and variation of water in DMD source material, the water loss of clasts of different size and with different durations of time above blocking temperature must be calculated. In this manner, an eruption of a certain grain size distribution and initial water content can be modeled in order to calculate a numerical ESPAT transect that can be resolved with that of the DMD in order to find the initial water content that provides the best fit. The obstacle presented is that water loss is not only a function of clast size and total time spent above blocking temperature, but also previously unconstrained evaporation and cooling rates, as well as the initial concentration of water.

To constrain these evaporation and cooling rates and calculate water loss for clasts of different sizes experiencing different cooling histories, we expand the work of *Saal et al.* [2008]. They introduced an innovating new method in which the composition of pyroclastic source material could be investigated by modeling diffusion profiles of volatile species F, Cl, S, and H₂O recorded in Delano's green glasses. These profiles within a single bead are a function of the clast size, evaporative and cooling environments, total time spent above blocking temperature, and initial concentration of the given volatile species. Following the lowering of the detection threshold for H₂O and CO₂ by virtue of secondary ion mass spectrometry (SIMS), *Saal et al.* [2008] were able to detect for the first time measurable amounts of H₂O and CO₂, as well as Cl, F, and S, in

a single glass bead (Delano’s green glass bead #5) which decreased from core to rim within the bead. Our expansion on the work of *Saal et al.* [2008] shows that the solution to the concentration profiles in the beads is non-unique and can be fitted satisfyingly for a broad range of total time above the blocking temperature because of trade-offs between cooling time, cooling and evaporation rates (see two examples of simulations for 10 and 300 seconds of evaporation in **figures s1 -4**). However, we find that the profiles can only be matched across a narrow range of evaporation and cooling rates (**figures s3 -4**) which provides constraints on these two parameters for the eruption that formed the deposits analyzed by Saal and coworkers. Both the cooling and evaporation rates are controlled to a first order by the environmental conditions sampled by the eruption. The DMDs investigated are presumed to be picritic in origin and emplaced through fire-fountaining eruptions, for which the environmental conditions are expected to share similarities with those of Delano’s glasses. From these constraints, we can calculate extreme water loss case scenarios using different combinations of evaporation rate and cooling rate determined from the fits to the data of *Saal et al.* [2008].

To calculate the diffusion profiles of the different chemical species, we solve for the diffusion of water in a sphere with radiation at the surface, described using Eq. (s1) [*Crank* , 1975]:

$$\frac{\partial C}{\partial t} = \frac{D(T)}{r^2} \frac{\partial}{\partial r} (r^2 \frac{\partial C}{\partial r}) \text{ (s1)}$$

where C is the concentration of the given volatile species (F, Cl, S, or H_2O), D is the temperature, and therefore time, dependent diffusivity, t is time spent above blocking temperature, and r is the distance along the radius of the clast. Using an implicit, centered-space, finite-difference approximation, Eq. (s1) can be written as:

$$\frac{C_k^{n+1} - C_k^n}{t} = \frac{2D}{r} \left[\frac{C_k^{n+1} - C_{k-1}^{n+1}}{r} \right] + D \left[\frac{C_{k+1}^{n+1} - 2C_k^{n+1} + C_{k-1}^{n+1}}{(r)^2} \right] \text{ (s2)}$$

where k is used to index position within the clast along the radius and n is used to index time in cooling history.

The boundary and initial conditions for this problem are:

$$\frac{\partial C}{\partial r} |_{r=R} = \frac{-\beta}{D(T)} (C - C_o) \text{ (s3)}$$

$$\frac{\partial C}{\partial r} |_{r=0} = 0 \text{ (s4)}$$

$$C(r, 0) = C_{ini} , \text{ (s5)}$$

with β being the species dependent evaporation rate, C_o being the initial concentration of the volatile species at the surface of the clast, here assumed to be negligible, and C_{ini} being the initial concentration of a given volatile species within the clast.

The inputs of forward diffusion calculations are the total time of diffusion, t_{total} , the radius of the clast, R , the evaporation rate β , and the rate of cooling [*Crank* , 1975]. These calculations are made simultaneously for all four species and we use a Markov Chain Monte-Carlo approach to find the optimal set of evaporation and cooling rates that satisfy these profiles. The diffusion coefficients and activation energies used in the inversion are reported in *Watson and Bender* [1980] for Cl, *Zhang and Stolper*[1991] for H_2O , and *Dingwell and Scarfe*[1984] for F. For S, we use the assumption made in *Saal et al.* [2008] that the sulfur partitions primarily as S^2 at low f_{O_2} [*Baker and Rutherford* , 1996] and that the activation energy should be similar to that of O^{2-} reported in *Wendlandt*[1991]. Finally, the diffusion coefficient for S is taken to be that reported in *Saal et al.* [2008].

Markov chain Monte Carlo:

The Markov chain Monte Carlo (MCMC) is based on a random walk through parameter space where new steps are either rejected or accepted on the basis of maximizing the likelihood of the model to fit our dataset (here ESPAT profiles). A MCMC realization includes a burn-in period where successive iterations lead to a subdomain of the parameter space close to the most likely solution. After the burn-in period, the algorithm samples randomly the parameter distributions around the best solution. While there is no definitive way

to determine the convergence of an MCMC model, one of the diagnostics that can be employed that may suggest convergence are trace plots and post burn-in marginal posteriori distributions and covariance plots. Plotting this results in distinctive trace or “caterpillar” plots where the model samples a given parameter until it converges upon the solution space. The trace plots and post burn-in marginal posteriori distributions and covariance plots for each of the DMDs investigated are provided in **figure s3 -4** .

The calculation of the error between the observed ESPAT, \mathbf{f} , and that of the model, \mathbf{p} , is calculated as:

$$L_k = \sum (\mathbf{f} - \mathbf{p}_k)^2 \quad (\text{s6})$$

where k is the k^{th} step in the Monte Carlo chain. The calculation of \mathbf{p} is performed based on \mathbf{m} , a perturbation to an initial proposal of model parameters written in vector form as \mathbf{m} (Eq. (1) & (16) in the main text). The new candidate vector, \mathbf{m}' , is then accepted in the chain and saved as \mathbf{m} for the next step if the criteria below is met:

$$\zeta > \log(\varepsilon) \quad (\text{s7})$$

where ε is a number sampled from a random uniform distribution between 0 and 1 and ζ is defined as:

$$\zeta = \gamma\varphi \quad (\text{s8})$$

where γ is an arbitrary pre-factor and φ is defined as:

$$\varphi = -L_{k-1} + L_k \quad (\text{s9})$$

In this way, if the error is lowered between successive steps, the new candidate vector is accepted as the next step in the chain. If the error is not lowered, there is still a probability that the candidate vector will be accepted in order to escape local extrema. The acceptance rate, defined as the percent of accepted candidate vectors \mathbf{m}' during the duration of the Markov chain, optimizes the MCMC inversion when between values of ~20% for higher dimensional problems [Roberts *et al.* , 1997], which can be achieved by adjusting the pre-factor γ until a proper acceptance rate is achieved. A similar method was also used to perform MCMC inversions for the fitting of data from Saal *et al.* [2008] in order to constrain the evaporation and cooling rates [Roberts *et al.* , 1997].

Hosted file

image2.emf available at <https://authorea.com/users/540818/articles/606421-modeling-lunar-pyroclasts-to-probe-the-volatile-content-of-the-lunar-interior>

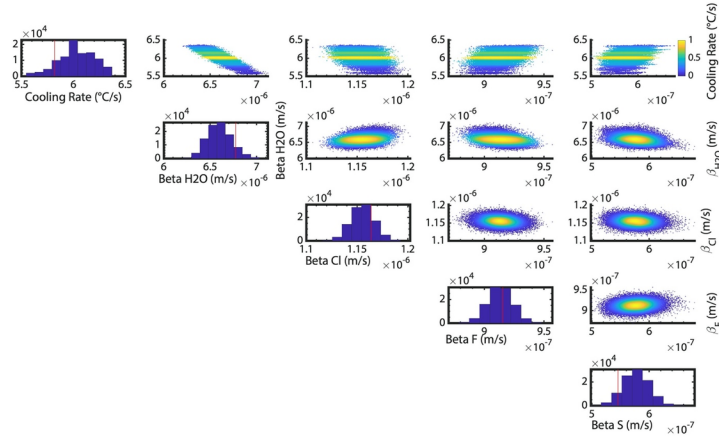
Supplement figure 1: Data from Saal *et al.* [2008] for H₂O, F, Cl, and S measured in Delano’s green glass #5, fit for a total time spent above blocking temperature of 10 s. Values of β and cooling rates that resulted in the best fit are listed in the panels. Fits are obtained performing a MCMC inversion.

Supplement figure 2: Data from Saal *et al.* [2008] for H₂O, F, Cl, and S measured in Delano’s green glass #5, fit for a total time spent above blocking temperature of 300 s. Values of β and cooling rates that resulted in the best fit are listed in the panels. Fits are obtained performing a MCMC inversion.

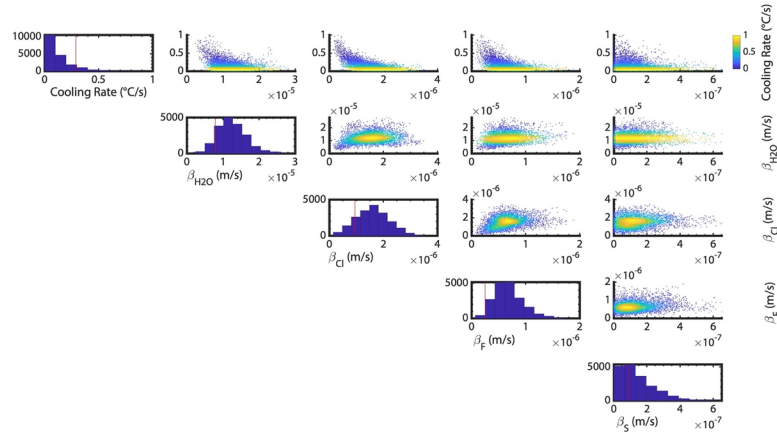
Hosted file

image3.emf available at <https://authorea.com/users/540818/articles/606421-modeling-lunar-pyroclasts-to-probe-the-volatile-content-of-the-lunar-interior>

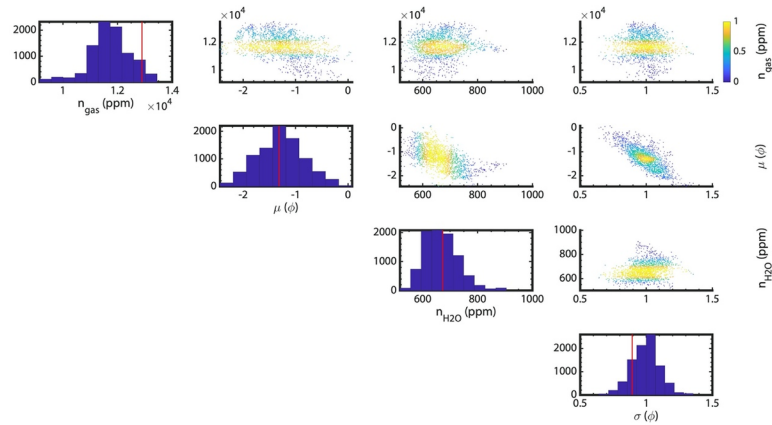
Supplement figure 3: Results of MCMC fitting diffusion data of Saal *et al.* [2008] with a fixed total time spent above blocking temperature of 25 seconds.. Along diagonal of matrix of plots is the marginal posteriori distribution for each parameter of the diffusion model with the solid red line representing the most likely solution in the parameter space, while the off-diagonal scatter plots highlight the covariance between parameters sampled from the posteriori distribution after burn-in.



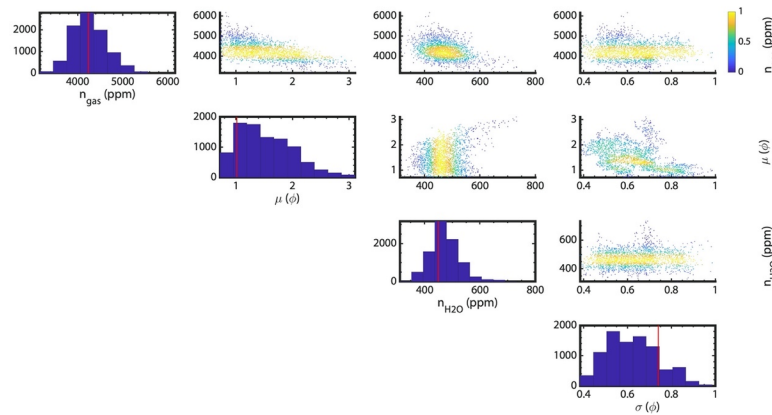
Supplement figure 4: Results of MCMC fitting diffusion data of *Saal et al.* [2008] with a fixed total time spent above blocking temperature of 300 seconds.. Along diagonal of matrix of plots is the marginal posteriori distribution for each parameter of the diffusion model with the solid red line representing the most likely solution in the parameter space, while the off-diagonal scatter plots highlight the covariance between parameters sampled from the posteriori distribution after burn-in.



Supplement figure 5: Results of MCMC for DMD Grimaldi I. Along diagonal of matrix of plots is the marginal posteriori distribution for each parameter of the eruption-diffusion model with the solid red line representing the most likely solution in the parameter space, while the off-diagonal scatter plots highlight the covariance between parameters sampled from the posteriori distribution after burn-in.



Supplement figure 6: Results of MCMC for DMD Birt E. Along diagonal of matrix of plots is the marginal posteriori distribution for each parameter of the eruption-diffusion model with the solid red line representing the most likely solution in the parameter space, while the off-diagonal scatter plots highlight the covariance between parameters sampled from the posteriori distribution after burn-in.



References

- Baker, L., and M. J. Rutherford (1996), Sulfur diffusion in rhyolite melts, *Contributions to Mineralogy and Petrology* , 123 (4), 335-344.
- Crank, J. (1975), *The Mathematics of Diffusion*: Oxford University, *New York* , 19752 , 1-21.
- Dingwell, D. B., and C. M. Scarfe (1984), Chemical diffusion of fluorine in jadeite melt at high pressure, *Geochimica et Cosmochimica Acta* , 48 (12), 2517-2525.
- Roberts, G. O., A. Gelman, and W. R. Gilks (1997), Weak convergence and optimal scaling of random walk Metropolis algorithms, *The annals of applied probability* , 7 (1), 110-120.
- Saal, A. E., E. H. Hauri, M. L. Cascio, J. A. Van Orman, M. C. Rutherford, and R. F. Cooper (2008), Volatile content of lunar volcanic glasses and the presence of water in the Moon's interior, *Nature* , 454 (7201), 192-195.

Watson, E., and J. Bender (1980), Diffusion of cesium, samarium, strontium, and chlorine in molten silicate at high temperatures and pressures, paper presented at Geol. Soc. Am. Abstr. Program.

Wendlandt, R. F. (1991), Oxygen diffusion in basalt and andesite melts: experimental results and discussion of chemical versus tracer diffusion, *Contributions to Mineralogy and Petrology* , 108 (4), 463-471.

Zhang, Y., and E. M. Stolper (1991), Water diffusion in a basaltic melt, *Nature* , 351 (6324), 306-309.

Modeling Lunar Pyroclasts to Probe the Volatile Content of the Lunar Interior

Darien Florez¹, Christian Huber¹, Ralph Milliken¹, Julia Berkson¹

¹Brown University, Department of Earth, Environmental and Planetary Sciences
Contact: darien_florez@brown.edu

1. Abstract

Constraining the volatile budget of the lunar interior has important ramifications for models of Moon formation. While many early and previous measurements of samples acquired from the Luna and Apollo missions suggested the lunar interior is depleted in highly volatile elements like H, a number of high-precision analytical studies over the past decade have argued that it may be more enriched in water than previously thought. Here, we integrate recent remotely sensed near-infrared reflectance measurements of several Dark-Mantle-Deposits (DMDs), interpreted to represent pyroclastic deposits, and physics-based eruption models to better constrain the pre-eruptive water content of lunar volcanic glasses. We model the trajectory and water loss of pyroclasts from eruption to deposition, coupling eruption dynamics with a volatile diffusion model for each pyroclast. Modeled pyroclast sizes and final water contents are then used to predict spectral reflectance properties for comparison with the observed orbital near-infrared data. We develop an inversion scheme based on the Markov-Chain Monte-Carlo (MCMC) method to retrieve constraints between governing parameters such as the initial volatile content of the melt and the pyroclast size distribution (which influences the remotely measured water absorption strengths). The MCMC inversion allows us to estimate the primordial (pre-eruption) water content for different DMDs and test whether their source is volatile-rich. Our results suggest that the parts of the lunar interior sampled by the source material of the DMDs investigated in this study range in water content from 400 to 800 ppm.

2. Introduction

Volatile elements, in particular hydrogen (e.g., in the form of OH/H₂O, hereafter referred to simply as ‘water’ or H₂O), affect planetary processes via their control over magma viscosity, mineral stability, and magma eruption dynamics [Asimow *et al.*, 2003; Gaetani and Grove, 1998; Hirth and Kohlstedt, 1996].

Although several different competing models exist, several models of lunar formation that have recently gained momentum in the planetary science community involve to an extent the giant impact theory (see, for example, the terrestrial synestia model of Lock *et al.* [2018]). In this giant impact theory, the Moon is thought to have been formed from the coalescence of debris from a collision between an impactor and a proto-Earth [Canup, 2004], leading to the formation of a lunar magmatic ocean and the large-scale degassing of the Moon [Lucey *et al.*, 2006]. The depletion of water in volcanic samples returned from Luna and Apollo missions seemed to support this, but a growing body of research now suggests that the lunar mantle, or at least some parts of the lunar mantle, may not be as severely depleted in water as previously thought [Boyce *et al.*, 2010; Greenwood *et al.*, 2011; Hauri *et al.*, 2011; Hui *et al.*, 2017; McCubbin *et al.*, 2010a; McCubbin *et al.*, 2010b; Rutherford *et al.*, 2017; Saal *et al.*, 2008; Saal *et al.*, 2013].

Much of the uncertainty surrounding the character of the lunar interior stems from the availability of direct samples from the lunar surface being limited to only a small number of locations. However, telescopic and other remote sensing observations have revealed so-called

49 Dark Mantle Deposits (DMDs) to be distinct features across the lunar surface [*L Gaddis et al.*,
50 1998; *L R Gaddis et al.*, 2000; *L R Gaddis et al.*, 1985; *L R Gaddis et al.*, 2003; *Gustafson et al.*,
51 2012; *Head*, 1974; *Weitz et al.*, 1998]. Although no large DMD has ever been sampled, and in
52 general their relation to the specific pyroclastic materials returned from the Luna and Apollo
53 missions is unclear, they are interpreted to be pyroclastic in nature and, if true, represent magmas
54 sourced from the deep lunar interior [*L R Gaddis et al.*, 1985; *Head*, 1974; *Weitz et al.*, 1998].

55 Most recent work using lunar samples to robustly constrain the water content of the lunar interior
56 has focused on picritic glasses [*Hauri et al.*, 2011; *Rutherford et al.*, 2017; *Saal et al.*, 2008; *Saal*
57 *et al.*, 2013]. These glasses are thought to have been emplaced through Hawaiian-like, fire-
58 fountaining eruptions [*Wilson and Head III*, 2003] and include green (low Ti), yellow
59 (intermediate Ti), and orange, red, and black glasses (high Ti). They represent quenched melts
60 that are ultramafic in composition [*J W Delano*, 1986; *Saal et al.*, 2008], crystal poor [*J W*
61 *Delano*, 1986; *Saal et al.*, 2008], were erupted as fine beads (< 1 mm) [*J W Delano*, 1986; *G*
62 *Heiken and McKay*, 1977; *Longhi*, 1992; *Saal et al.*, 2008; *Weitz et al.*, 1998], and are believed
63 to have been generated from magmas sourced at depths of 300 - 500 km [*J Delano*, 1980; *J*
64 *Delano and Lindsley*, 1983; *Elkins et al.*, 2000; *Elkins-Tanton et al.*, 2003; *Longhi*, 2006; *C*
65 *Shearer and Papike*, 1993; *C K Shearer et al.*, 2006]. For this reason, they have been used to
66 probe the volatile content of parts of the lunar interior by virtue of melt inclusions, diffusion
67 modeling, and through solubility experiments [*Hauri et al.*, 2011; *Rutherford et al.*, 2017; *Saal et*
68 *al.*, 2008; *Saal et al.*, 2013].

69 Volatile content profiles of individual picritic glass beads were first reported by *Saal et al.*
70 [2008], where improvements in secondary ion mass spectrometry allowed for lower detection
71 threshold for water. These improvements led to the detection of measurable amounts of water
72 (up to 46 ppm), and *Saal et al.* [2008] found systematic depletion from core to rim within
73 individual beads. These volatile profiles suggest the beads degassed during ascent and eruption
74 [*Saal et al.*, 2008], consistent with a volcanic (as opposed to impact) origin. The trace amount of
75 water detected in these glasses therefore represents the concentration of water in the parental
76 magma upon fragmentation after magmatic degassing.

77
78 Magmatic degassing is assumed to take place as fragmented pyroclasts travel through a
79 thermally opaque, water undersaturated, gas cloud during their ballistic trajectory [*Wilson and*
80 *Keil*, 2012]. The volatile profiles recorded by these pyroclasts during this process are therefore
81 modulated by the cooling time (i.e. the time spent traveling through the opaque gas cloud), the
82 size and shape of the pyroclast, and the pre-eruption magmatic volatile content, as well as the
83 conditions (rate) above the blocking temperature [*Crank*, 1975]. Here, the blocking temperature
84 is generally assumed to be the melt-glass transition temperature for the volatile species
85 considered. Based on these relationships, the volatile profiles measured in the pyroclasts can be
86 used to constrain the range of values for these different parameters. For instance, *Saal et al.*
87 [2008] applied the measured volatile content values to a degassing/diffusion model and estimated
88 the initial amount of water upon magma fragmentation to be within the range of 260 to 15,000
89 ppm [*Saal et al.*, 2008] (94.0% and 99.9% percent water loss, respectively), with a best-fitting
90 solution of 745 ppm (98% water loss). Though even the lowest model values have a significant
91 implication for the volatile budget of the Moon, this is a broad range and the solution is clearly
92 not unique. Therefore, further constraints are desired to help narrow down the range of possible

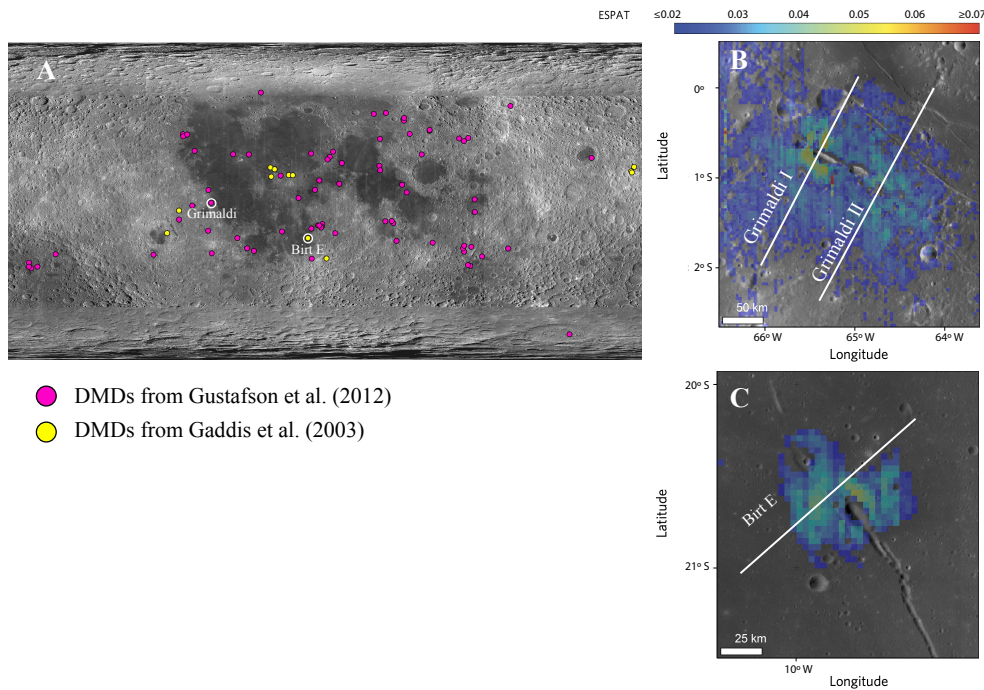
93 solutions and provide useful estimates of mantle volatile composition in the source magmas that
94 feed pyroclastic eruptions on the Moon.

95
96 One useful additional constraint is, when possible, to locate the vent(s) associated with a
97 pyroclastic deposit. The size of a pyroclastic deposit and the distance from the point of origin
98 (vent) provides information on the trajectory of the pyroclasts and thus their cooling time above
99 the blocking temperature. Unfortunately, specific vents associated with glass beads returned
100 from the Luna and Apollo sampling sites are not apparent in existing data. However, remotely
101 sensed data such as images from NASA's Lunar Reconnaissance Orbiter have revealed the
102 presence of vents for several small DMDs elsewhere on the lunar surface [*Gustafson et al.*,
103 2012]. In addition, near-infrared reflectance spectra acquired by the Moon Mineralogy Mapper
104 (M3) imaging spectrometer on the Chandrayaan-1 spacecraft have revealed that nearly all DMDs
105 on the Moon exhibit spectral signatures indicative of enhanced water contents, including several
106 of the small DMDs with visible vents [*Li and Milliken, 2017; Ralph E Milliken and Li, 2017*].

107
108 The M3 reflectance spectra, in conjunction with laboratory measurements and radiative transfer
109 models, were used to estimate the amount of water in the DMDs based on the strength of an
110 OH/H₂O absorption feature at a wavelength of ~2.7-2.9 μm [*Ralph E Milliken and Li, 2017*].
111 The parameter used to characterize the absorption strength was the Effective Single Particle
112 Absorption Thickness (ESPAT) as described and defined by [*Hapke et al., 1993*]. Previous
113 studies have shown that the ESPAT parameter is linearly correlated with water content for a
114 wide range of hydrous materials, but the slope of that linear relationship varies with the particle
115 size of the material [*Li and Milliken, 2017; Ralph Edward Milliken, 2006; Ralph E Milliken and*
116 *Mustard, 2005; 2007a; b*]. In order to estimate the current (post-emplacment) water content of
117 the DMDs, *Ralph E Milliken and Li [2017]* assumed the deposits were spectrally dominated by
118 particles (pyroclasts) ~60-80 μm in diameter. The main challenges with this approach are (1) that
119 the pyroclast size distribution of the deposits as a whole, as well as the pyroclast size distribution
120 with distance from the vent, are unknown, and (2) that volatile diffusion profiles for glass beads
121 within these deposits are unavailable and therefore can't be used to independently determine the
122 pre-fragmentation water content.

123
124 In this study we seek to determine if there exist a suite of conditions for which analytical
125 measurements of lunar glasses, physical eruption models, and remotely sensed measurements of
126 pyroclastic deposits yield self-consistent results for water in lunar DMDs. That is, can pyroclast
127 size distributions and water content values estimated from an eruption model be used to predict
128 the range of possible absorption strengths (ESPAT values) that might be observed in near-
129 infrared reflectance spectra and are these in agreement with the values reported in Milliken and
130 Li (2017)? Alternatively, do eruption models predict pyroclast sizes significantly larger or
131 smaller than assumed in that previous study and, if so, what does this imply about quantifying
132 water content of DMDs using near-infrared reflectance data such as M³? To address these issues
133 and further constrain pre-fragmentation water content of lunar magmas, we develop a new
134 approach using eruption dynamics together with volatile diffusion out of pyroclasts. Near-IR
135 ESPAT values are expected to vary as a function of both water content and pyroclast size [*Li and*
136 *Milliken, 2017; Ralph E Milliken and Li, 2017*]. As such, transects of ESPAT values from a
137 DMD vent to its perimeter are expected to vary based on differences in pre-fragmentation water
138 content, pyroclast size, and the exsolved gas content that accelerates the pyroclasts to their

139 eventual deposition. All three of these critical parameters can be independently evaluated in a
 140 physics-based eruption model, and we use ESPAT profiles measured across several small DMDs
 141 with vents to find a solution space that results in fits to the ESPAT profiles while simultaneously
 142 satisfying the dynamics of large fire fountain volcanic events on the Moon. To accomplish this,
 143 we develop an approach that requires calculating water loss through magmatic diffusion in
 144 pyroclasts and the loss is calculated here using new constraints from diffusion modeling of
 145 analytically measured picritic glasses similar to that of *Saal et al.* [2008]. This study represents
 146 the first time that analytical measurements of lunar glasses, a physics-based eruption model, and
 147 remote sensing observations of lunar water absorptions have all been integrated to better
 148 constrain the amount of water in lunar DMDs and their magma source regions.



149
 150 **Figure 1.** A Map of Dark Mantle Deposits (DMDs) in and around Procellarum KREEP Terrain identified from
 151 *Gustafson et al.* [2012] and *L R Gaddis et al.* [2003]. DMDs Grimaldi and Birt E (investigated in this study) are
 152 circled in white. B + C ESPAT maps and approximate transect lines of DMDs Grimaldi and Birt E, respectively.
 153

154 3. Methods

155 To investigate the volatile budget of DMD source material, we couple an eruption model for
 156 pyroclast dispersal with a diffusion model to account for volatile loss during pyroclast transport
 157 above the blocking temperature. The pyroclast sizes and water contents that are output by the
 158 model are used to predict the near-IR ESPAT values that would be observed in the M3 data
 159 (described in detail below), where the ESPAT values are a quantitative measure of the OH/H₂O
 160 absorption strength near a wavelength of ~2.9 μm and whose derivation is described in *Ralph E*
 161 *Milliken and Li* [2017] and *Li and Milliken* [2017]. We use maps of ESPAT values previously
 162 published by *Ralph E Milliken and Li* [2017] and *Li and Milliken* [2017] to extract transects of
 163 ESPAT values over two small DMDs with identifiable vents: Birt E and Grimaldi [*Ralph E*
 164 *Milliken and Li*, 2017] (**figure 1**). The eruption dynamics model solves for the depth of magma
 165 fragmentation, which depends on the exsolved volatile content of the magma rising to the
 166 surface, and the ballistic trajectory of *n* pyroclasts of a certain size (diameter) distribution and
 167 pre-eruptive water content. The volatile loss experienced by each of the *n* pyroclasts is calculated

168 with a diffusion model calibrated on the data of *Saal et al.* [2008]. This allows us to generate a
169 map of pyroclast size and post-diffusion water content as function of distance from the vent and
170 thus construct synthetic ESPAT value maps for the two DMDs. The free parameters in the model
171 are the pre-fragmentation water content of the rising magma, the concentration of exsolved
172 volatiles at fragmentation, and pyroclast size distribution. The misfit between the synthetic
173 (modeled) and measured ESPAT values of the DMD's are calculated and a Markov-Chain
174 Monte-Carlo is implemented in order to retrieve the parameters that result in the best models (i.e.
175 the most probable model parameters). Although the actual areal extent and even the
176 corresponding source vents of many lunar DMDs may be obscured by younger mare deposits
177 [*Head, 1974*], the inversion is preformed such that the model fits the entire ESPAT transect, and
178 thus makes no assumptions of the deposit size other than that it is smaller than the length of the
179 transect itself. Using this technique, we can ascertain the most probable pre-eruptive water
180 content, concentration of exsolved gas upon fragmentation, as well as pyroclast size distribution
181 parameters that reproduce the observed water absorption strengths (ESPAT values) for the
182 deposits of interest. Definitions for all variables used by the model are provided in **table 1** below.
183

Symbol	Definition	Units
n_{H_2O}	mass fraction of pre-fragmentation water	
n_{gas}	mass fraction of exsolved volatiles at fragmentation	
μ	mean pyroclast size	ϕ
σ	pyroclast size standard deviation	ϕ
d	diameter of pyroclast	m
\bar{d}	average pyroclast size of deposit	m
R	radius of pyroclast	m
Q_u	universal gas constant, 8.314×10^3	$J \text{ kmol}^{-1} \text{ K}^{-1}$
ρ_l	density of picritic magma	kg/m^3
m	molar mass of exsolved gas at fragmentation	$kg/kmol$
T_m	temperature of melt	K
P_{frag}	fragmentation pressure	Pa
P_{ch}	choked flow pressure at vent	Pa
U_v	vent velocity of gas and perfectly coupled pyroclasts	m/s
P_f	final pressure gas expands to	Pa
N_a	Avogadro's number	mol^{-1}
ϕ_{gas}	effective gas molecule diameter, $\sim 3.4 \times 10^{-10}$	m
U_f	velocity of gas and perfectly coupled particles at P_f	m/s

u_t	terminal velocity of pyroclasts	m/s
U_b	initial ballistic velocities for pyroclasts	m/s
X	dimension of thermally opaque gas cloud	m
R_f	maximum range for pyroclastic deposit	m
F_e	erupted volume flux of magma from fissure vent	m ³ /s
t_{dike}	total time pyroclasts spend in dike post fragmentation	s
t_{cloud}	total time pyroclasts spend in gas cloud post dike	s
t_{total}	total time pyroclasts spend diffusing	s
C^i	concentration of volatile species i	ppm
β^i	evaporation rate for chemical species i	m/s
D^i	temperature dependent diffusivity for chemical species i	m ² /s
D_o^i	diffusion coefficient for chemical species i	m ² /s

Table 1. Table summarizing symbols for coefficients used in model calculations.

2.1 Eruption model

We simulate the eruption and deposition of n pyroclasts using the eruption model of *Wilson et al.* [2010], *Wilson and Keil* [2012], *Wilson and Head III* [2003], *Wilson and Head* [2017], and *Head and Wilson* [2017], with model parameters \mathbf{m} . Here, \mathbf{m} can be written as:

$$\mathbf{m} = [n_{H_2O}, n_{gas}, \mu, \sigma] \quad (1)$$

where n_{H_2O} is the initial concentration of H₂O in DMD parental magma upon fragmentation, n_{gas} is the concentration of the mixture of exsolved gas driving the eruption upon fragmentation, and μ and σ are the mean and standard deviation of the pyroclast size distribution. Here μ and σ are expressed in terms of Φ , where Φ is related to pyroclast size diameter, d , in mm as [*Krumbein*, 1934; *Mueller et al.*, 2019]:

$$d = 2^{-\Phi} . \quad (2)$$

Using a lognormal relationship between Φ and wt% as implemented by *Mueller et al.* [2019], we generate a pyroclast size distribution for n pyroclasts ($n = 40,000$ for simulations presented in **table 2**). Given pyroclast size parameters μ and σ , representing the mean and standard deviation of the deposit in terms of Φ , the fraction of the arbitrary population that any given pyroclast size comprises and the resulting average pyroclast size can be calculated.

The composition of the gas mixture exsolved from lunar picritic magmas upon fragmentation are best constrained using melt inclusion and glass data, as well as solubility experiments performed

209 on orange (high-Ti) lunar glass beads [Fogel and Rutherford, 1995; Rutherford et al., 2017;
 210 Wetzel et al., 2015; Wetzel et al., 2013]. These studies suggest that the orange picritic glasses
 211 fragmented at a depth of 300 – 600 m, based on considerations of the concentration of C
 212 dissolved in melt inclusions. Taking this into account, we use the composition of the exsolved
 213 gas phase of the picritic magma at depths of 300 – 600 m, as calculated by Rutherford et al.
 214 [2017] corresponding to 115 ppm CO, 10 ppm H₂O, 18 ppm S₂, 34 ppm SO₂, 19 ppm H₂S, and
 215 10 ppm F.

216
 217 To solve for the pyroclasts' trajectory, we first calculate the pressure (and depth) at which the
 218 rising magma is disrupted and transitions from a melt with suspended gas into a gas with
 219 suspended melt droplets by assuming a critical volume fraction of gas as 0.85 using the ideal gas
 220 law:

$$221 \quad P_{frag} = \frac{0.15 n_{gas} Q_u T_m \rho_l}{0.85(1-n_{mix})m} \quad (3)$$

222
 223 where P_{frag} is the disruption pressure, n_{gas} is the mass fraction of exsolved volatiles, Q_u is the
 224 universal gas constant (8.314kJ kmol⁻¹ K⁻¹), T_m is the magmatic temperature, ρ_l is the density of
 225 the liquid phase, and m is the molar mass of the volatile mixture [Wilson and Head, 2017]. The
 226 magmatic temperature here is assumed to be 1450 °C, slightly above the maximum liquidus of
 227 the green picritic glasses which ranges from 1405 to 1448 °C [J Delano, 1990]. This assumption
 228 is supported by the fact that most picritic glasses tend to be crystal poor [Elkins-Tanton et al.,
 229 2003].
 230

231
 232 The pyroclasts are assumed to be perfectly coupled to the gas and therefore travel and accelerate
 233 with the gas as it expands to the choked flow conditions at the vent, P_{ch} , which can be calculated
 234 iteratively as Wilson and Head [2017]:
 235

$$236 \quad \frac{n_{gas} Q_u T_m}{m} \ln \frac{P_{frag}}{P_{new}} + \frac{1-n_{gas}}{\rho_l} (P_{frag} - P_{old}) = P_{old}^2 \frac{m}{2 n_{gas} Q_u T_m} \frac{n_{gas} Q_u T_m}{m P_{old}} + \frac{1-n_{gas}^2}{\rho_l} \quad (4)$$

237
 238 With knowledge of the pressure of disruption and the pressure at the vent from Eq. (4), the total
 239 time that the newly formed pyroclasts spend at high temperatures while being transported in the
 240 dike/conduit, t_{dike} , can be calculated using the Simpson integration rule [Atkinson, 1989] and
 241 integrating from the fragmentation depth to the surface.
 242

243 From P_{ch} obtained from Eq. (4), the averaged vent velocity, U_v , can be approximated as:
 244

$$245 \quad 0.5 U_v^2 = \frac{n_{gas} Q_u T_m}{m} \ln \frac{P_{frag}}{P_{ch}} + \frac{1-n_{gas}}{\rho_l} (P_{frag} - P_{ch}) - \left(\frac{P_{frag} - P_{ch}}{\rho_c} \right) \quad (5)$$

246
 247 using the arguments from Wilson [1980] and Wilson and Head [2017], where ρ_c is the density of
 248 the lunar crust, 2550 kg m⁻³ [Wieczorek et al., 2013]. Next, the final pressure, P_f , at which the gas
 249 expands to outside of the vent can be calculated using Eq. (6), which depends on the average
 250 pyroclast size of the eruption [Wilson and Head, 2017; Wilson et al., 2010]. Pyroclasts that are

251 perfectly coupled will inherit the velocity of the gas as it expands to P_f , where P_f is calculated as
 252 [*Wilson and Head, 2017; Wilson et al., 2010*]:

$$254 \quad P_f = \frac{2^{0.5} Q_u T_m}{3 \pi \varphi^2 N_a \bar{d}} \quad (6)$$

255
 256 where φ is the effective diameter of the gas molecules, 3.4×10^{-10} m for CO, \bar{d} is the average
 257 pyroclast size, and N_a is Avogadro's number, 6.0225×10^{26} kmol⁻¹. At this point the
 258 expanding gas reaches a velocity of, U_f , calculated as [*Wilson and Head, 2017*]:

$$260 \quad 0.5 U_f^2 = 0.5 U_v^2 + \frac{n_{gas} Q_u T_m}{m} \ln \frac{P_{ch}}{P_f} + \frac{1 - n_{gas}}{\rho_l} [P_{ch} - P_f] \quad (7)$$

261
 262 The terminal velocity, u_t , by which the pyroclasts lags behind the expanding gas due to drag is
 263 calculated as [*Wilson et al., 2010*]:

$$265 \quad u_t = \left(\frac{4 d \rho_c g}{3 C_d \rho_g} \right)^{0.5} \quad (8)$$

266
 267 where the Reynolds number is assumed to be large enough to be turbulent. Therefore, the initial
 268 ballistic velocity of each bead, U_b , can be calculated as:

$$270 \quad U_b = U_f - u_t \quad (9)$$

271
 272 From this point, the pyroclasts experience uninterrupted ballistic trajectory until deposition.
 273 Under conditions that may allow for an opaque gas cloud to form at the vent and thermally
 274 insulate the pyroclast, we compute the extent of that opaque cloud, X , from the maximum range
 275 of the pyroclasts following the treatment of *Wilson and Keil* [2012] for a fissure-like vent:

$$277 \quad X = R_f - \frac{6.17 \bar{d} R_f^{2.5}}{F_e} \quad (10)$$

278
 279 The fissure-like geometry is assumed here to most closely reflect the shape of the inferred vents
 280 of the DMDs investigated in this study (**figure 1**). From the extent of the opaque gas cloud, the
 281 time each pyroclasts spent in the hot gas cloud, t_{cloud} , can be calculated and added to the time
 282 each pyroclast spends traveling in the dike post-fragmentation, t_{dike} , to compute the total time
 283 that each pyroclast spends above the closing temperature and experiences volatile loss by
 284 diffusion

$$286 \quad t_{total} = t_{dike} + t_{cloud} \quad (11)$$

288 2.2 Diffusion model

289 To determine the fraction of water remaining in each pyroclast after being deposited, we solve
 290 for the diffusion of water in a sphere with radiation at the surface according to the diffusion
 291 equation [*Crank, 1975*]:

292

293
$$\frac{\partial C}{\partial t} = \frac{D(T)}{r^2} \frac{\partial}{\partial r} \left(r^2 \frac{\partial C}{\partial r} \right) \quad (12)$$

294
 295
$$\frac{\partial C}{\partial r} \Big|_{r=R} = \frac{-\beta}{D(T)} (C - C_o) \quad (13)$$

296

297 using an implicit, centered-space, finite-difference approximation. Further details of the
 298 discretization can be found in the supplementary text. The inputs to this diffusion model are the
 299 total time of diffusion, t_{total} , the size of the pyroclast, d , the evaporation rate β , and the rate of
 300 cooling [Crank, 1975]. The time for diffusion and the pyroclast size are determined from the
 301 eruption model through Eq. (2) and Eq. (10), while the evaporation rate and cooling rate remain
 302 unconstrained. We expand upon the work of Saal *et al.* [2008] to constrain these parameters by
 303 finding the range of evaporation and cooling rates that give satisfactory fits to the core to rim
 304 volatile profiles of H₂O, F, Cl, and S measured in several lunar pyroclastic glass beads. These
 305 calculations are made simultaneously for all four species and we use a Markov Chain Monte-
 306 Carlo approach to find the optimal set of evaporation and cooling rates that satisfy these profiles
 307 (see Supplements). The diffusion coefficients and activation energies used in the inversion are
 308 reported in Watson and Bender [1980] for Cl, Zhang and Stolper [1991] for H₂O, and Dingwell
 309 and Scarfe [1984] for F. For S, we use the assumption made in Saal *et al.* [2008] that the sulfur
 310 partitions primarily as S² at low f_{O_2} [Baker and Rutherford, 1996] and that the activation energy
 311 should be similar to that of O²- reported in Wendlandt [1991]. Finally, the diffusion coefficient
 312 for S is taken to be that reported in Saal *et al.* [2008].

313 With these calculations, we can determine the upper and lower bounds of percent water loss: an
 314 upper limit using the highest H₂O evaporation rate and lowest cooling rate that provide
 315 satisfactory fits, and a lower bound by using the lowest H₂O evaporation rate and highest cooling
 316 rate that provided satisfactory fits. It is not entirely clear how formation and emplacement
 317 processes of the green picritic glasses, from which the diffusion constraints are obtained, relate to
 318 inferred pyroclasts at DMDs which we attempt to model. However, the DMDs are believed to be
 319 picritic as well, and the conditions for volatile diffusion and surface evaporation are presumed to
 320 be similar.

321

322 Combining the eruption model outputs with the volatile diffusion and loss model results, we then
 323 calculate values of water content and pyroclast size with distance from the vent of the two
 324 DMDs. The size and water content of pyroclasts distributed radially away from the vent can then
 325 be converted to ESPAT values in two steps. First, we can calculate the particle size effect on
 326 ESPAT with [Li and Milliken, 2017; Ralph E Milliken and Mustard, 2005; 2007b]):

327

328
$$\text{slope} = 0.6608 + 4.7067 \exp(-0.04352 d) \quad (14)$$

329

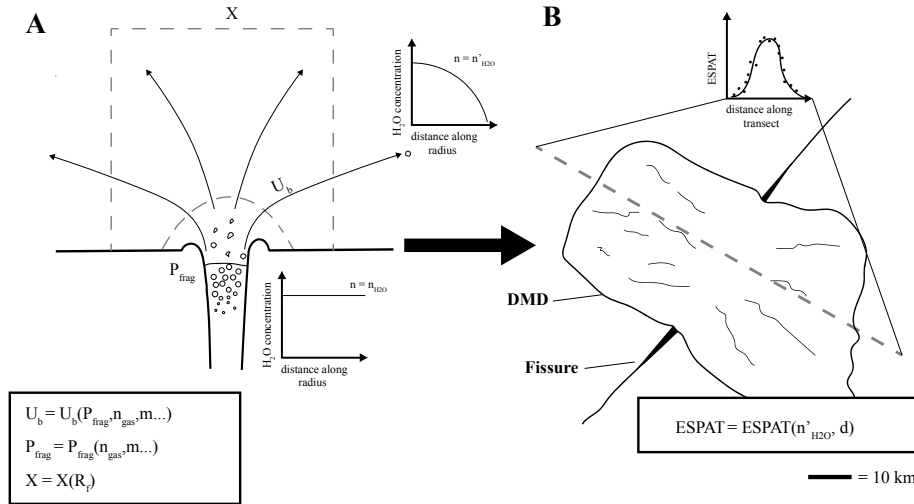
330 where *slope* refers to the slope of the linear relationship between ESPAT values and water
 331 content, which varies with particle size (d). The ESPAT values are then calculated based on the
 332 water content from the eruption and diffusion model [Li and Milliken, 2016; 2017; Ralph E
 333 Milliken and Li, 2017; Ralph E Milliken and Mustard, 2007b]:

334

335
$$\text{ESPAT} = \frac{1}{\text{slope}} \text{wt \% H}_2\text{O} \quad (15)$$

336
 337
 338
 339
 340
 341
 342

This approach is, in effect, a forward model of the near-IR water absorption strength based on the absorption path length (particle size) and concentration of the absorbing species (water content). The modeled ESPAT values can then be compared with the actual ESPAT value profiles from the M3 data and the parameters in the eruption model that result in the best fit can be determined. A schematic summary of the eruption-diffusion model is provided below in **figure 2**.



343
 344
 345
 346
 347

Figure 2. Schematic rendering of the eruption-diffusion model. **A** Schematic of critical stages of eruption model and how they depend on model parameters. **B** Schematic of resulting numerical ESPAT that results from the simulated eruption.

348 2.3 Markov chain Monte Carlo inversion

349 The section above describes the flow chart to run (forward) a realization of a synthetic ESPAT
 350 profile away from a vent. The next step is to develop a non-linear optimization scheme to find
 351 the free parameters, **m**

352

$$353 \quad m = [n_{H_2O}, n_{gas}, \mu, \sigma] \quad (16)$$

354

355 that minimize the residual between the numerically simulated ESPAT profile and that of the
 356 measured DMD. The optimization is performed with a Markov chain Monte Carlo (MCMC)
 357 method. The MCMC is an inversion technique for non-linear problems and allows sampling of
 358 the posterior distribution of the model parameters of interest [Anderson and Segall, 2013]. The
 359 chain samples the posterior distribution by perturbing the model parameter vector **m** by a random
 360 amount in order to obtain **m'**. In this way, the future state of the chain obeys a Markovian
 361 process and depends only on the present state of the process when using the MCMC [Anderson
 362 and Segall, 2013]. From **m'**, the forward eruption and water loss models are run and the ESPAT
 363 of the resulting deposit is calculated. If the residual is lowered between successive iterations, the
 364 new model parameters **m'** are saved and replace **m** for the next iteration. If the *residual* (L2-
 365 norm of the difference between observed and modeled ESPAT profiles) is not lowered, we
 366 compute the difference in likelihood between the solutions of the 2 consecutive iterations and use
 367 it to calculate the probability that the parameters of the last iteration are accepted. This finite
 368 probability allows a candidate vector, **m'**, that may fail to lower the residual to still be accepted
 369 and allow the model to escape local extrema [Anderson and Segall, 2013]. This sequence is

370 repeated for N iterations until the posterior distribution has been adequately sampled (in this
 371 study $N \sim 20,000$ - $40,000$ iterations are sufficient to draw good statistics from the posteriori
 372 distributions).

373
 374 **3. Results**

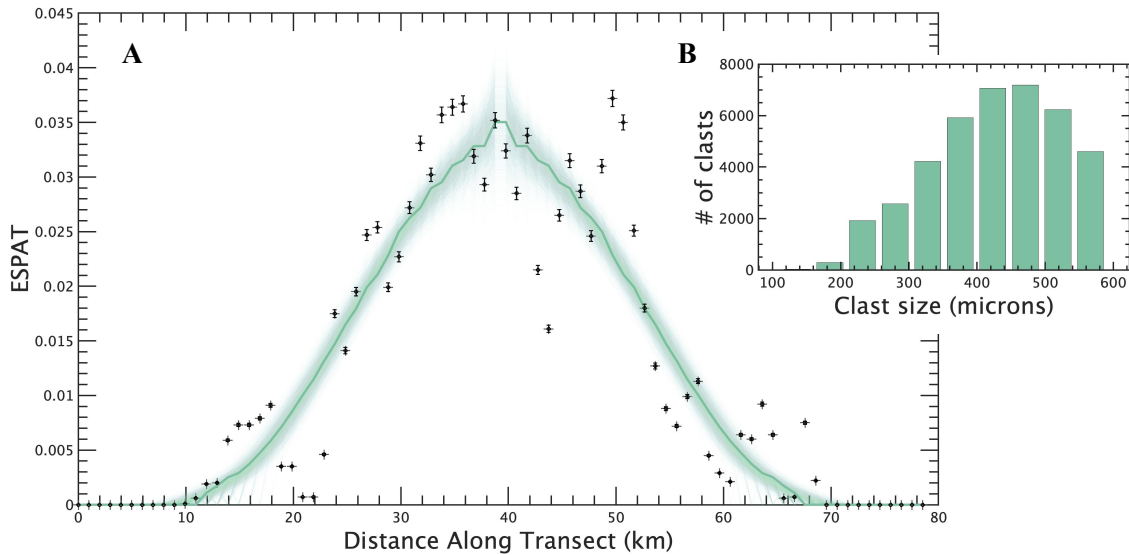
375 In order to obtain the upper and lower bounds of each parameter of the coupled eruption-water
 376 diffusion model, we explore the following scenarios: pyroclast diffusion calculations with
 377 boundary conditions that enhance water loss (corresponding to an evaporation rate of 3.5×10^{-5}
 378 m/s and a cooling rate of $0.1 \text{ }^\circ\text{C/s}$), as well as boundary conditions that limit water loss
 379 (corresponding to an evaporation rate of 1.4×10^{-6} m/s and a cooling rate of $6.4 \text{ }^\circ\text{C/s}$). These
 380 bounds are obtained from fitting diffusion profiles in the Apollo 15 green glasses measured by
 381 *Saal et al.* [2008]. Intermediate combinations of these boundary conditions are also explored and
 382 tabulated in **table 2**. The two DMDs investigated are Grimaldi, for which two ESPAT transects
 383 were evaluated (Grimaldi I and Grimaldi II), and Birt E. The measured ESPAT profiles for
 384 Grimaldi II are left unaltered, but some of the ESPAT values measured in the transects Grimaldi
 385 I and Birt E are not taken into account when calculating the misfit during the MCMC. Further
 386 details and justification about this omission can be found in the Discussion section. The modeled
 387 ESPAT profiles agree closely with ESPAT transects of the two DMDs (**figure 3, 5**). Parameters
 388 converged upon by the MCMC are summarized in **table 2**. Trace and covariate plots for different
 389 MCMC runs suggest convergence, with a burn-in period of ~ 1000 - 2000 iterations, depending on
 390 the initial seeds of the Markov chain **figure 4**.

391

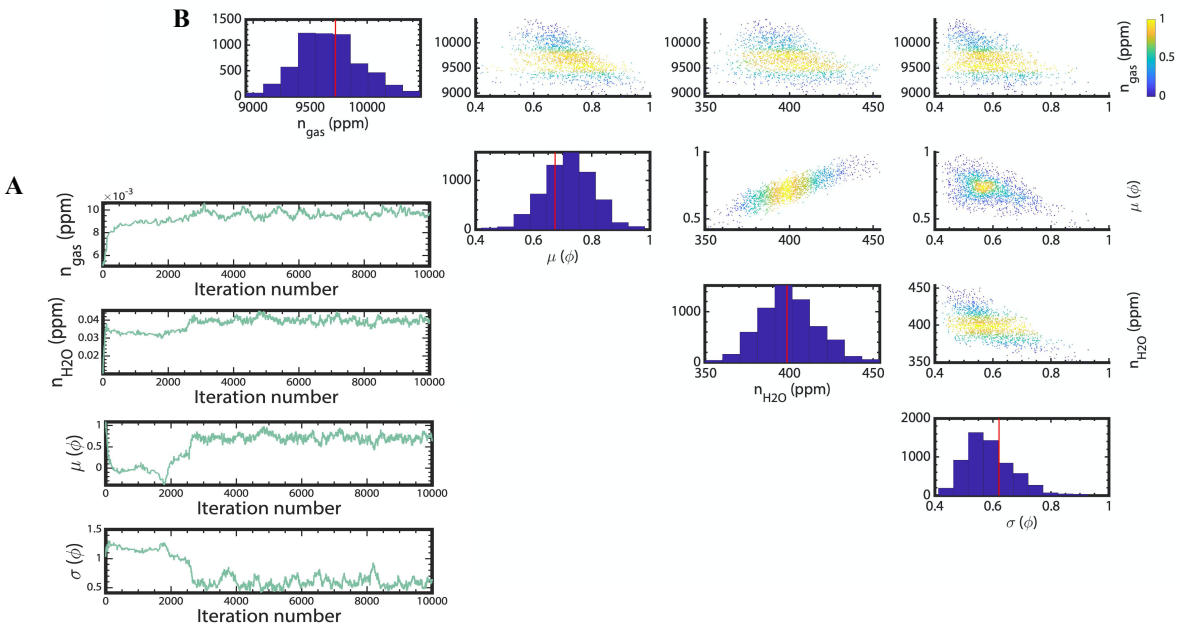
DMD	n_{gas} (ppm)	$n_{\text{H}_2\text{O}}$ (ppm)	σ (phi)	μ (Φ)/ d_{50} (μm)	n_{gas} (ppm)	$n_{\text{H}_2\text{O}}$ (ppm)	σ (phi)	μ (phi)	Evaporation rate (m/s)	Cooling rate ($^\circ\text{C/s}$)
Grimaldi II	9932 +/- 308	412 +/- 18	0.46	0.76/410	9800	400	0.49	0.74	1.4×10^{-6}	6.4
Grimaldi II	15,025 +/- 1,213	674 +/- 103	0.35	0.36/626	16,282	621	0.3	0.15	3.5×10^{-5}	6.4
Grimaldi II	9,745 +/- 614	400 +/- 16	0.55	0.71/372	5,000	100	1	1	1.4×10^{-6}	6.4
Grimaldi II	13,342 +/- 1,154	585 +/- 50	0.34	0.47/575	14,098	560	0.34	0.39	3.5×10^{-5}	0.1
Grimaldi II	14,314 +/- 1,322	773 +/- 135	0.38	0.46/573	15,342	704	0.34	0.33	1.4×10^{-6}	0.1
Grimaldi II	6,696 +/- 395	246 +/- 16	0.81	0.31/306	5,000	100	1	1	1.4×10^{-6}	6.4
Grimaldi II	7,290 +/- 224	266 +/- 10	1.06	-1.10/ 310	6,913	252	0.8	0.02	1.4×10^{-6}	0.1
Grimaldi II	12,612 +/- 1,264	507 +/- 53	0.38	0.48/565	12,267	512	0.41	0.56	3.5×10^{-5}	6.4
Grimaldi II	13,032 +/- 887	580 +/- 37	0.40	0.5/530	11,612	573	0.63	0.67	3.5×10^{-5}	0.1
Grimaldi I	29,038 +/- 1,788	805 +/- 152	0.79	-1.87/ 1,439	21,465	1,159	0.9	-2.08	1.4×10^{-6}	0.1
Grimaldi I	52,304 +/- 1,896	1317 +/- 244	0.20	-1.04/ 1,865	21,465	1,159	0.9	-2.08	3.5×10^{-5}	0.1
Grimaldi I	11,167 +/- 789	681 +/- 63	1.03	-1.29/ 545	11,310	634	0.9	-0.78	1.4×10^{-6}	6.4
Grimaldi I	21,480 +/- 1,535	1151 +/- 127	0.96	-2.1/ 1,058	21,465	1,159	0.9	-2.08	3.5×10^{-5}	6.4
Grimaldi I	7,226 +/- 3,3,938	497 +/- 118	1.12	-1.5/ 473	7,207	470	1.06	-0.92	1.4×10^{-6}	0.1
Grimaldi I	23,291 +/- 1,774	1138 +/- 576	0.8	-1.6/ 1,179	21,465	1,159	0.9	-2.08	3.5×10^{-5}	0.1
Grimaldi I	6,891 +/- 409	474 +/- 35	1.13	-1.59/ 1,495	7,106	481	0.96	-0.98	1.4×10^{-6}	6.4

Grimaldi I	19,490 +/- 983	1055 +/- 103	0.92	-2.09/ 1,265	21,465	1,159	0.9	-2.08	3.5×10^{-5}	6.4
Birt E	5,490 +/- 856	505 +/- 58	0.62	0.34/1,265	4,397	522	0.76	0.78	1.4×10^{-6}	0.1
Birt E	6998 +/- 58	910 +/- 48	1.77	-2.33/53	4,397	522	0.76	0.78	3.5×10^{-5}	0.1
Birt E	4,642 +/- 371	459 +/- 54	0.47	1.26/291	4,397	522	0.76	0.78	1.4×10^{-6}	6.4
Birt E	12,076 +/- 1,317	962 +/- 197	0.18	0.36/713	4,397	522	0.76	0.78	3.5×10^{-5}	6.4
Birt E	4,649 +/- 256	420 +/- 47	0.72	0.38/363	4,172	468	0.78	0.61	1.4×10^{-6}	0.1
Birt E	6,959 +/- 400	982 +/- 102	0.82	0.96/195	8,000	911	0.69	0.65	3.5×10^{-5}	6.4
Birt E	4,776 +/- 552	448 +/- 51	0.69	0.45/356	4,397	422	0.76	0.78	1.4×10^{-6}	6.4
Birt E	7,168 +/- 454	1188 +/- 143	0.76	0.93/214	4,397	522	0.76	0.78	3.5×10^{-5}	0.1

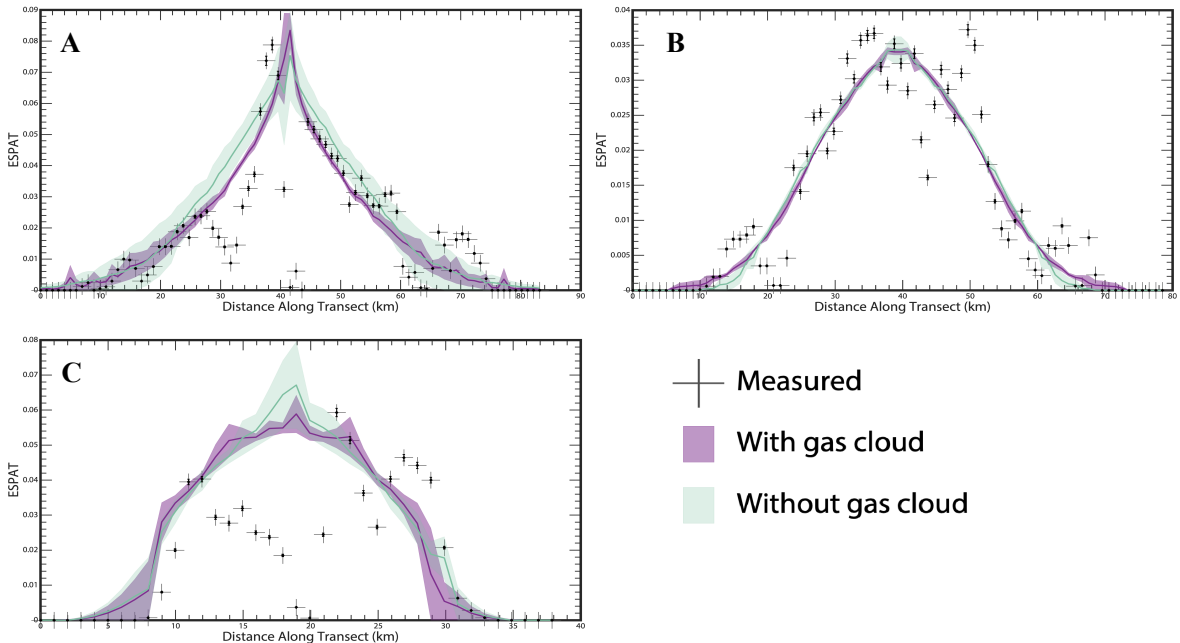
392 **Table 2.** Table summarizing all of the MCMC runs performed in this study. Runs in light blue indicate simulations
 393 with out a thermally opaque gas cloud. Parameters highlighted in grey indicate initial starting values for each
 394 MCMC while parameters to the left of the highlighted region indicate the parameters that result in the best fit for
 395 each run.



396 **Figure 3.** **A** The solid line represents the best fitting model for the second transect for the DMD Grimaldi II for an
 397 MCMC run of 10,000 iterations and an evaporation rate of 1.4×10^{-6} m/s and a cooling rate of 6.4 °C/s. The green
 398 shaded area brackets the resulting ESPAT profiles sampled after the burn-in period (~1000 iterations). **B** The
 399 resulting pyroclast size distribution for the best fitting model.
 400



401 **Figure 4.** **A** Trace plots for MCMC run on Grimaldi II with an evaporation rate of 1.4×10^{-6} m/s and a cooling rate
 402 of 6.4 °C/s. **B** Along diagonal of matrix of plots is the marginal posteriori distribution for each parameter with the
 403 solid red line representing the most likely solution in the parameter space, while the off-diagonal scatter plots
 404 highlight the covariance between parameters sampled from the posteriori distribution after burn-in.
 405



406 **Figure 5.** Best fitting models to the measured ESPAT profile for each combination of evaporation rate and cooling rate for **A** Grimaldi I, **B** Grimaldi II, and **C** Birt E. The solid line indicates the most likely solution, light shades
 407 indicate total range spanned by the posteriori distribution of the MCMC for inversions that include and neglect the
 408 presence of an opaque gas cloud.
 409
 410
 411

412 3.2 n_{H_2O}

413 Across all best fitting models for all of the DMDs, modeled with and without a thermally opaque
414 gas cloud, best-fitting models retrieve n_{H_2O} values that exhibit a total range from 246 +/- 16 ppm
415 to 1,317 +/- 244 ppm. The error bounds are calculated as the standard deviation of the
416 parameter's posteriori distribution sampled by the MCMC across the entire simulation after
417 burn-in.

418
419 The best-fit solutions for Grimaldi I correspond to n_{H_2O} values that range from 681 +/- 63 ppm to
420 1317 +/- 244 ppm when accounting for a thermally opaque gas cloud during the eruption
421 compared to the range from 474 +/- 35 ppm to 1138 +/- 576 ppm in the absence of a thermally
422 opaque gas cloud. The lower and upper bound values for both cases are obtained with the least
423 and most efficient water loss diffusion scenarios respectively. Comparatively, the n_{H_2O} values of
424 best-fitting models for Grimaldi II return ranges from 400 +/- 16 ppm to 773 +/- 135 ppm (with
425 gas cloud) and from 246 +/- 16 ppm to 580 +/- 37 ppm (without gas cloud). Finally, for Birt E,
426 the best solution yields n_{H_2O} values that range from 459 +/- 54 ppm to 962 +/- 197 ppm (with gas
427 cloud) and from 420 +/- 47 ppm to 1188 +/- 143 ppm (without gas cloud). Additionally, for each
428 DMD, we see that the returned pre-fragmentation concentrations of water, n_{H_2O} , consistently
429 increase as evaporation rate increases and cooling rate decreases **table 2**. For all of the DMDs,
430 all else equal, the presence of a thermally opaque gas cloud results in higher pre-fragmentation
431 water content (n_{H_2O} values).

432 433 3.3 n_{gas}

434 Best-fitting models for all of the DMDs, both with and without a thermally opaque gas cloud,
435 return corresponding n_{gas} values that exhibit a range from 4,642 +/- 371 ppm to 52,304 +/- 1,896
436 ppm. The range of n_{gas} values for each individual DMD both with and without a thermally
437 opaque gas cloud can be found in **table 2**.

438
439 For each DMD, we see that the returned exsolved gas concentration upon fragmentation, n_{gas} , are
440 also positively correlated with the inferred evaporation rate and negatively correlated with the
441 cooling rate **table 2**. For the range of n_{gas} values returned, the corresponding confining pressure
442 at the level of fragmentation range from ~1 – 11 MPa. The lower end of this range corresponds
443 to models run for the less extensive Birt E deposit (~39 km transect) considering low evaporation
444 rates and high cooling rates, whereas the higher end corresponds to the longer Grimaldi I transect
445 (~85 km) and an assumption of high evaporation rates and low cooling rates **table 2**. In all cases
446 modeled, except for Birt E with an evaporation rate of 1.4×10^{-6} m/s and a cooling rate of 6.4
447 °C/s, the presence of a thermally opaque gas cloud implies lower n_{gas} values (**table 2**).

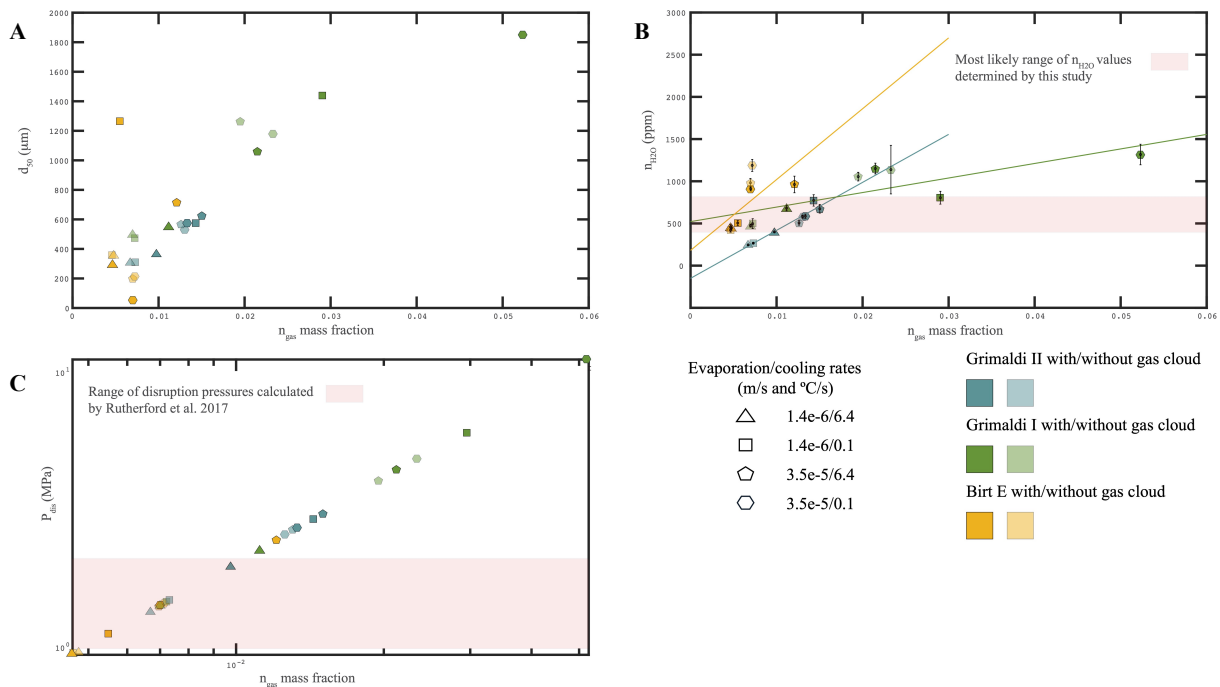
448 449 3.4 Pyroclast size distribution μ and σ

450 For convenience, pyroclast size distribution is discussed in terms of the best-fitting models of
451 pyroclast size in units of micrometers that corresponds to the 50th percentile of the size
452 distribution, d_{50} . Across all best fitting models for all of the DMDs, modeled with and without a
453 thermally opaque gas cloud, d_{50} ranges from 53 to 1,865 μm . The range of d_{50} values for each
454 individual DMD both with and without a thermally opaque gas cloud can be found in **table 2**.
455 For each DMD, with few exceptions, the pyroclast size corresponding to the 50th percentile is
456 positively correlated to evaporation rate and negatively correlated to cooling rate.

457

458 **4. Discussion**

459 Of the three DMD transects that were modeled, Grimaldi II exhibits a complete, continuous, and
 460 symmetric spatial ESPAT distribution, and thus offers the most robust constraints for the
 461 eruption-diffusion model (**figure 1**). Asymmetry in the ESPAT maps and profiles (**figure 1, 5**)
 462 can be explained in several ways, including an angled conduit at the lunar surface, non-uniform
 463 topography, and uneven weathering or overlap of a younger unit. Additionally, Grimaldi I and
 464 Birt E both have ESPAT values of zero at the inferred vent, which is where one would expect
 465 ESPAT values to be highest as the largest pyroclasts are deposited near the vent and retain more
 466 water. Lower ESPAT values at or near the vent could possibly be explained by significant water
 467 loss for particles remaining within a thermally opaque cloud throughout the transport and
 468 perhaps even shortly after deposition. Alternatively, M3 pixels (spectra) directly over and
 469 adjacent to the vents can have low signal due to shadowing effects (e.g., see shadows for Birt E
 470 in Figure 1), which can result in falsely low values. Small-scale shadowing effects due to small
 471 impact craters and impact excavation of anhydrous material that lies beneath the DMD material
 472 may also explain some of the pixel-to-pixel variability in ESPAT values along the transects, such
 473 as some of the low points observed in Figure 5A for Grimaldi I. For simplicity, we omit these
 474 anomalous data points towards the center of the Grimaldi I and Birt E transects and focus instead
 475 on the tails of the ESPAT distribution away from the vent as they are more sensitive to eruption
 476 dynamics and pyroclast size distribution. Despite this omission, the range of values returned for
 477 each parameter for the three modeled ESPAT transects show significant overlap. To our
 478 knowledge, these results offer tighter constraints on these parameters for lunar pyroclastic
 479 eruptions and associated magma source regions than previously offered [*Hauri et al., 2011*;
 480 *Rutherford et al., 2017*; *Saal et al., 2008*; *Saal et al., 2013*]. Importantly, the results also
 481 demonstrate that reasonable values for these parameters can be achieved that both fit the
 482 remotely sensed near-IR data and are consistent with current pyroclastic eruption models.



483 **Figure 6.** The parameters that resulted in the best fitting models for each MCMC run are plotted here. **A** Pyroclast
 484 size corresponding to the 50th percentile, **B** wt % H₂O pre-fragmentation, and **C** fragmentation pressure vs mass
 485

486 fraction of exsolved gas at fragmentation. The range highlighted in panel C corresponds to the range of
487 fragmentation depths for the orange picritic glasses determined petrologically by [Rutherford *et al.*, 2017].
488

489 4.1 n_{H_2O}

490 For a given ESPAT transect, as one considers a scenario that would enhance water loss (slower
491 cooling rate or higher evaporation rate), the best fit model parameters are adjusted by increasing
492 the amount of pre-fragmentation water such that the quality of the ESPAT profile fit is
493 maintained (**table 2**). A satisfactory fit can be found for each combination of evaporation and
494 cooling rate applied to each transect, but the only overlap in solution space in terms of pre-
495 fragmentation water content between all three DMD transects occurs in a narrow range from
496 ~400 – 800 ppm **figure 6**.

497
498 For Grimaldi, considering both transects, the range for pre-fragmentation water content likely
499 ranges from ~400 – 800 ppm on the basis of the overlap in n_{H_2O} solution space both with and
500 without gas cloud, or ~500 – 600 ppm if considering only the scenarios without a thermally
501 opaque gas cloud (**table 2; figure 6**). Because Grimaldi I and II were transects measured across
502 the same DMD, the true pre-fragmentation water returned by the eruption-diffusion model
503 should agree. Assuming the presence of a thermally opaque gas cloud, the only models for both
504 Grimaldi I and II that fall within this overlapping solution space are the scenario with an
505 evaporation rate of 1.4×10^{-6} m/s and 6.4 °C/s (**figure 6; table 2**). For models without a
506 thermally opaque gas cloud, no combination of evaporation rate and cooling rate returns n_{H_2O}
507 values that fall within a common range for both Grimaldi I and II (**figure 6, table 2**). This may
508 suggest the presence of a thermally opaque gas cloud at Grimaldi.
509

510 For Birt E, the best fitting models for the same evaporation rate of 1.4×10^{-6} m/s and cooling
511 rates of either 0.1 and 6.4 °C/s also return pre-fragmentation water concentrations consistent with
512 that of Grimaldi, 400 – 800 ppm (**figure 6; table 2**), while n_{H_2O} values for best fitting models
513 with an evaporation rate of 3.5×10^{-5} m/s and either a cooling rate of 0.1 or 6.4 °C/s yield higher
514 values from 910 to 1188 ppm. While the n_{H_2O} values returned for Birt E that were obtained
515 assuming high evaporation rates could be explained by the presence of spatial heterogeneities in
516 the distribution of water in DMD source material, the values for n_{H_2O} remain within the range
517 modeled for Grimaldi I (**figure 6; table 2**). Because of this, it is likely that the pre-fragmentation
518 water content in these DMD source materials is similar and that the evaporation rate during lunar
519 eruptions tends towards values closer to that of 1.4×10^{-6} m/s, at least for eruptions with a
520 thermally opaque gas cloud.
521

522 The most likely range of water contents determined in this study (400 – 800 ppm) is in good
523 agreement with the most likely range of water contents previous studies have reported for parts
524 of the lunar interior sampled by the lunar picritic glasses (260 – 745 ppm; Saal *et al.* [2008], 615
525 – 1410 ppm; Hauri *et al.* [2011]). Our results support the growing body of work that suggests
526 parts of lunar interior are more enriched in volatiles than previously thought [Hauri *et al.*, 2011;
527 Rutherford *et al.*, 2017; Saal *et al.*, 2008; Saal *et al.*, 2013]. Source magma water content
528 inferred from the ESPAT values calculated for the DMDs studied here suggest a maximum range
529 of 246 – 1317 ppm (**figure 6; table 2**). These values are a lower bound as they don't take into
530 account any water lost from outgassing pre-fragmentation. We note however, that the data from
531 olivine melt inclusions in Apollo 17 orange glass beads suggest a very small H_2O fraction in the
532 pre-fragmentation gas phase. Additionally, these values may not be representative of the bulk

533 lunar mantle as the lunar glasses are believed to be generated from partial melting of
534 differentiated and likely volatile enriched LMO material [*J W Delano, 1986; Hess and*
535 *Parmentier, 1995; C K Shearer et al., 2006*], and the degree of partial melting is estimated to be
536 5-10% [*Saal et al., 2008*].

537 538 4.2 n_{gas}

539 The exsolved gas concentration upon fragmentation, n_{gas} , exerts important controls over the
540 model and, ultimately, the fit to the observed ESPAT data. The value of n_{gas} directly influences
541 the depth of fragmentation, the size of the thermally opaque gas cloud (if any), the trajectories of
542 the pyroclasts forming the deposit, and consequently the extent of water loss by degassing. As
543 water loss is enhanced, the values of n_{gas} that result in the closest ESPAT fits tend to increase
544 (**table 2**). This is largely because at a fixed n_{gas} , the distribution of pyroclasts away from the vent
545 remains identical but enhanced water loss decreases the calculated ESPAT values across the
546 profile. To counteract this effect and retrieve an acceptable fit to observed ESPAT profiles, the
547 solution space is shifted towards a larger pyroclast size distribution (i.e., if the concentration of
548 the absorbing species decreases then the absorption path length must increase to maintain the
549 same absorption strength). To enable the larger pyroclasts to travel the same distance, the n_{gas}
550 must increase so that the pyroclasts inherit enough kinetic energy to match the extent of the
551 observed water signature in the near-IR data.

552
553 For the range of n_{gas} values returned, the corresponding pressure at the fragmentation level ranges
554 from $\sim 1 - 11$ MPa (**figure 6**). Considering the Grimaldi models with overlapping solution space
555 as well as all of the best fitting models for Birt E, this range reduces to $\sim 1-3$ MPa (**figure 6;**
556 **table 2**). This lower range is in close agreement with values determined from petrological studies
557 using C dissolved in melt inclusions in picritic orange glasses that suggest fragmentation at $\sim 1-2$
558 MPa [*Rutherford et al., 2017*]. We reiterate that the composition of the exsolved gas at
559 fragmentation used for the models is that reported by *Rutherford et al. [2017]*, with a molar mass
560 of 36 g/mol. To investigate the dependence of our results on the composition of the exsolved gas,
561 for the least efficient water loss conditions applied to Grimaldi II, two additional MCMCs were
562 run: one with an arbitrary molar mass of exsolved gas of 20 g/mol and with 65 g/mol. Assuming
563 a molar mass for the gas mixture of 65 g/mol, we find that the disruption pressure is decreased
564 by less than 0.1 MPa and the pre-fragmentation water content reduced from 400 to 340 ppm.
565 Using instead 20 g/mol, the disruption pressure is increased by ~ 0.5 MPa and the pre-
566 fragmentation water content is increased from 400 to 520 ppm. This range in possible molar
567 masses for a given composition of exsolved gas represents extreme upper and lower bounds and
568 seems to suggest that the composition does not significantly alter the results.

569
570 As determined by *Rutherford et al. [2017]* based on gas solubility experiments and analyses of
571 the orange picritic glasses, the abundance of exsolved gas at the transition from equilibrium to
572 kinetic degassing is too low to lead to magma fragmentation. Using C values measured in the
573 orange picritic glass, *Rutherford et al. [2017]* estimate the depth of fragmentation to be within
574 300 – 600 m from the surface (1-2 MPa), and therefore determine that there is a contribution
575 from open system degassing. The concentration of exsolved volatiles at fragmentation returned
576 by our models are in excess of those calculated by *Rutherford et al. [2017]* for closed system
577 degassing. The difference between the values of n_{gas} returned by our model and the closed-
578 system degassing calculated by *Rutherford et al. [2017]* (~ 200 ppm) represents the contributions

579 from open-system degassing. The inability of closed-system degassing to cause fragmentation at
580 depths that agree with those determined petrologically by *Rutherford et al.* [2017] in the orange
581 picritic glasses as well as the large n_{gas} values determined in this study can at least in part be
582 explained by the dike-tip propagation model of lunar glass formation proposed by *Head and*
583 *Wilson* [2017]. In this model, efficient open system degassing allows a volatile-rich foam to form
584 at the tip of a propagating dike and propels the orange picritic glass magma to the lunar surface.
585

586 4.3 Pyroclast size distribution μ and σ

587 The pyroclast size distribution affects the ballistic trajectory of the pyroclast, the loss of volatiles
588 by diffusion, and also directly influences the modeled ESPAT values. This effect of pyroclast
589 size on water loss can be seen as models trade-off between pyroclast size and the assumed
590 conditions for water loss (evaporation and cooling rates). Models run under conditions that do
591 not favor volatile retention (high evaporation rates and low cooling rates) return larger average
592 pyroclast size distributions because larger pyroclasts retain water more readily than smaller
593 pyroclasts (**figure 6; table 2**). Furthermore, the lateral extent of the modeled deposits depends on
594 the pyroclast size distribution because smaller pyroclasts inherit a greater proportion of the
595 momentum of the expanding gas cloud, which explains the positive correlation between average
596 pyroclast size and mass fraction exsolved gas at fragmentation.
597

598 Across all of the best models, the returned pyroclast size distributions are such that d_{50} ranges
599 from 53 to 1,865 μm (**figure 6; table 2**). When considering the added constraints for the
600 fragmentation depth from *Rutherford et al.* [2017], this range reduces to 53 to 1,265 μm (**figure**
601 **6**). For Grimaldi, when considering only the models with parameters that overlap for Grimaldi I
602 and II, the range in pyroclast sizes is further reduced to 372 - 626 μm (**figure 6; table 2**). For Birt
603 E, the total range in pyroclast sizes (again 50th percentile) range from 53 to 1,265 μm for the
604 best fitting models (**figure 6; table 2**). Despite the large range in pyroclast sizes determined by
605 the inversion calculation, the solutions with the highest likelihood agree with the observation that
606 the picritic glasses are submillimeter (<1 mm) [*G H Heiken et al.*, 1991; *Rutherford et al.*, 2017;
607 *Saal et al.*, 2008].
608

609 4.3 Constraints on evaporation and cooling rate

610 In addition to each of the parameters constrained by this work, we find that the combinations of
611 evaporation rate and cooling rate that provide mutual satisfactory fits to the two Grimaldi
612 transects only occur at low evaporation rates (10^{-6} m/s) (**figure 6; table 2**), in agreement with the
613 low evaporation rates determined experimentally by *Arndt et al.* [1984], and with the diffusion
614 profiles modeled numerically by *Saal et al.* [2008]. However, we find that only cooling rates
615 slightly above the range determined by *Saal et al.* [2008] ($<5^{\circ}\text{C/s}$) provide model results that
616 agree between the two Grimaldi transects (6.4 $^{\circ}\text{C/s}$) (**figure 6; table 2**) for models with a gas
617 cloud. In fact, for Grimaldi I, for either evaporation rate of 1.4×10^{-6} or 3.5×10^{-5} m/s, with a
618 cooling rate of 0.1 $^{\circ}\text{C/s}$, a satisfactory fit with ESPAT data cannot be provided when accounting
619 for a thermally opaque gas cloud. This is because under these enhanced water loss conditions the
620 average pyroclast size corresponding to best fitting models needs to be large in order to limit
621 water loss, and consequently (**table 1**) the size of the thermally opaque gas cloud vanishes in Eq.
622 (9). ESPAT values for the Birt E transect, however, can be adequately fit using any combination
623 of evaporation rate (either 1.4×10^{-6} m/s or 3.5×10^{-5} m/s) and cooling rate (0.1 or 6.4 $^{\circ}\text{C/s}$).
624 Moreover, all combinations for the water loss for Birt E provide reasonable fits within the

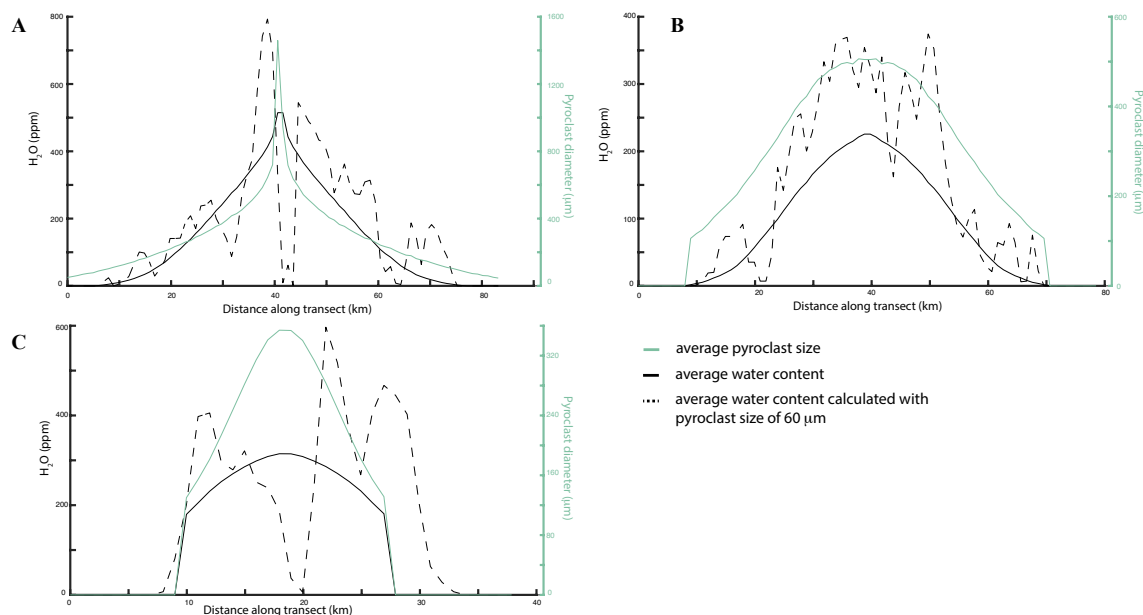
625 fragmentation depth constraints of *Rutherford et al.* [2017] (fractionation depths of 300 – 500 m)
626 (**figure 6; table 2**).

627

628 4.5 Agreement of n_{H_2O} and pyroclast size distribution with previous observations

629 The DMDs investigated in the present study are not related to the sites from which samples were
630 returned by the Apollo and Luna missions. The returned picritic glass samples display a typical
631 range of mean pyroclast size of 45 -100 μm [*G H Heiken et al.*, 1991; *Rutherford et al.*, 2017].

632 For the most probable best-fitting models, those that agree with the fragmentation depth
633 determined by *Rutherford et al.* [2017] as well as the models that provide agreement between the
634 two ESPAT transects for Grimaldi, the pyroclast size corresponding to 50th percentile range from
635 372 to 1,265 μm . This is larger than the range of average pyroclast sizes observed in the Apollo
636 soils [*G H Heiken et al.*, 1991]. The discrepancy can be attributed, at least in part, to the fact that
637 samples at or near a known vent have not been acquired. Samples from this region would contain
638 larger pyroclasts and potentially be less well-sorted.



639

640 **Figure 7.** Average pyroclast diameter determined and post-deposition water content from best-fitting models for **A**
641 Grimaldi I, **B** Grimaldi II, and **C** Birt E, along with water contents calculated similar to those of Milliken and Li
642 (2017) using fixed pyroclast diameter of 60 μm . Each of the best-fitting models here are for evaporation and cooling
643 rates of 1.4×10^{-6} m/s and 6.4 $^{\circ}\text{C/s}$, respectively.

644

645 4.6 Agreement distribution of water in lunar pyroclastic deposits reported in Milliken and Li 646 (2017)

647 The final distribution of water and average pyroclast diameter corresponding to each best-fitting
648 simulation with water-loss calculated with evaporation and cooling rates of 1.4×10^{-6} m/s and
649 6.4 $^{\circ}\text{C/s}$, respectively, are reported in **figure 7**. *Ralph E Milliken and Li* [2017] assumed the
650 DMDs investigated were spectrally dominated by particles (pyroclasts) ~ 60 - 80 μm in diameter in
651 order to the amount of water indigenous to the deposits. The results presented in this study
652 instead solve for pyroclast size and find that the pyroclast size distributions that result in the best-
653 fitting models are on average larger than that used in *Ralph E Milliken and Li* [2017], sometimes

654 by an order of magnitude. This results in the current DMD water contents reported in *Ralph E*
655 *Milliken and Li* [2017] to be, on average, higher than the results presented in this work. Despite
656 the large differences in pyroclast sizes (**figure 7**), the differences in the final water contents of
657 the DMDs is not huge and it is still clear that the DMDs are more hydrated than surrounding
658 regions. Most importantly, the results described here demonstrate that there exist a suite of
659 conditions for which the near-IR spectral data can be modeled and which are simultaneously
660 consistent with current eruption models. The integration of the models and the remotely sensed
661 data further support the notion that the magmas that gave rise to the DMDs are enriched in water.

662 **5. Conclusion**

663 Constraining the lunar volatile budget is important to further our understanding of lunar
664 formation and evolution as well as volcanic eruptions. Models of lunar formation and evolution
665 must be able to explain the retention of volatiles in parts of the lunar interior [*Hauri et al.*, 2011;
666 *Rutherford et al.*, 2017; *Saal et al.*, 2008; *Saal et al.*, 2013]. The present study offers constraints
667 on the pre-fragmentation water content of glass erupted and forming two Dark Mantle Deposits
668 (DMDs) where we can use spectral data to extract information about water content and pyroclast
669 size.

670
671 Our results suggest that the most likely range in water content in the glass before fragmentation
672 is 400 – 800 ppm. The most probable range of pre-fragmentation water contents for the very-low
673 Ti glasses is 260 – 745 ppm according to *Saal et al.* [2008] and 615 – 1410 ppm from *Hauri et*
674 *al.* [2011]. Our results are in close agreement with that of *Saal et al.* [2008], which provided the
675 data from which evaporation and cooling rate constraints were obtained, and is only slightly
676 lower than the range determined by *Hauri et al.* [2011]. This is likely because *Hauri et al.* [2011]
677 obtained the range in water content by analyzing dissolved water in melt inclusions, capturing
678 the trend of decreasing H₂O in trapped melt with decreasing pressure just prior to melt
679 fragmentation. The method used in this study not only provides tighter constraints on pre-
680 fragmentation water contents, but it also provides constraints for the concentration of exsolved
681 gas at fragmentation and constraints for the pyroclast size distribution of DMDs. The
682 concentration of exsolved volatiles at fragmentation according to our best-fitting models are in
683 excess of the concentrations calculated by *Rutherford et al.* [2017] assuming closed system
684 degassing. This supports their conclusion that open system degassing plays a significant role on
685 the eruption dynamics of these fire fountain eruptions and is in part explained by the dike
686 formation model of *Wilson and Head III* [2003] and *Head and Wilson* [2017].

687
688 The calculations for water loss use a range of evaporation and cooling rates obtained by fitting
689 diffusion data for the very low-Ti lunar glasses. Therefore, an important assumption this model
690 makes is that the diffusional environment for the pyroclasts associated with the DMDs being
691 investigated is similar to the very low-Ti, green lunar glasses. Additionally, the constraints on
692 fragmentation come from calculations made on the high-Ti, orange lunar glasses and may not be
693 applicable to the DMDs investigated here. The orange glasses are believed to have a higher
694 cooling rate than the other lunar glasses [*Arndt et al.*, 1984; *Arndt and Von Engelhardt*, 1987],
695 and if indeed the DMDs investigated here more closely represent the orange glasses, the pre-
696 fragmentation water content, the exsolved gas concentration at fragmentation, and the mean
697 pyroclast size returned by the best fitting models would likely decrease (**figure 6; table 2**).

699 Additional information on the titanium content of lunar DMDs could further constrain the results
700 presented here.

701
702 This study suggests that in the absence of new samples returned from the Moon, a combination
703 of remote sensing, numerical modeling, and petrology can be used to determine the composition
704 of the source material tapped by volcanic eruptions. The extent to which different parts of the
705 lunar interior may exhibit heterogeneous amounts of volatiles may not be entirely determinable
706 at present from the two DMDs investigated in this study, but the template presented here may
707 help fill in those gaps.

708 709 **6. Acknowledgements**

710 We greatly thank M.J. Rutherford, J.W. Head, and E. First for their ideas and guidance on this
711 project as well as their edits and reviews made on the manuscript. Codes are available and
712 archived at the Brown Digital Repository, Brown University Library,
713 <https://doi.org/10.26300/8pmw-yw23>.

714 715 **References**

- 716 Anderson, K., and P. Segall (2013), Bayesian inversion of data from effusive volcanic eruptions
717 using physics-based models: Application to Mount St. Helens 2004–2008, *Journal of*
718 *Geophysical Research: Solid Earth*, 118(5), 2017-2037.
- 719 Arndt, J., W. Engelhardt, I. Gonzalez-Cabeza, and B. Meier (1984), Formation of Apollo 15
720 green glass beads, *Journal of Geophysical Research: Solid Earth*, 89(S01), C225-C232.
- 721 Arndt, J., and W. Von Engelhardt (1987), Formation of Apollo 17 orange and black glass beads,
722 *Journal of Geophysical Research: Solid Earth*, 92(B4), E372-E376.
- 723 Asimow, P. D., Langmuir, and CH (2003), The importance of water to oceanic mantle melting
724 regimes, *Nature*, 421(6925), 815-820.
- 725 Atkinson, K. E. (1989), An introduction to numerical analysis *Rep.*
- 726 Baker, L., and M. J. Rutherford (1996), Sulfur diffusion in rhyolite melts, *Contributions to*
727 *Mineralogy and Petrology*, 123(4), 335-344.
- 728 Boyce, J. W., Y. Liu, G. R. Rossman, Y. Guan, J. M. Eiler, E. M. Stolper, and L. A. Taylor
729 (2010), Lunar apatite with terrestrial volatile abundances, *Nature*, 466(7305), 466-469.
- 730 Canup, R. M. (2004), Dynamics of lunar formation, *Annu. Rev. Astron. Astrophys.*, 42, 441-475.
- 731 Crank, J. (1975), The Mathematics of Diffusion: Oxford University, *New York, 1975*, 1-21.
- 732 Delano, J. (1980), Chemistry and liquidus phase relations of Apollo 15 red glass Implications for
733 the deep lunar interior, paper presented at Lunar and Planetary Science Conference Proceedings.
- 734 Delano, J. (1990), Buoyancy-driven melt segregation in the earth's moon. I-Numerical results,
735 paper presented at Lunar and Planetary Science Conference Proceedings.
- 736 Delano, J., and D. Lindsley (1983), Mare glasses from Apollo 17: Constraints on the Moon's
737 bulk composition, *Journal of Geophysical Research: Solid Earth*, 88(S01), B3-B16.
- 738 Delano, J. W. (1986), Pristine lunar glasses: Criteria, data, and implications, *Journal of*
739 *Geophysical Research: Solid Earth*, 91(B4), 201-213.
- 740 Dingwell, D. B., and C. M. Scarfe (1984), Chemical diffusion of fluorine in jadeite melt at high
741 pressure, *Geochimica et Cosmochimica Acta*, 48(12), 2517-2525.
- 742 Elkins, L., V. Fernandes, J. Delano, and T. Grove (2000), Origin of lunar ultramafic green
743 glasses: Constraints from phase equilibrium studies, *Geochimica et Cosmochimica Acta*, 64(13),
744 2339-2350.

745 Elkins-Tanton, L. T., N. Chatterjee, and T. L. Grove (2003), Experimental and petrological
746 constraints on lunar differentiation from the Apollo 15 green picritic glasses, *Meteoritics &*
747 *Planetary Science*, 38(4), 515-527.

748 Fogel, R. A., and M. J. Rutherford (1995), Magmatic volatiles in primitive lunar glasses: I. FTIR
749 and EPMA analyses of Apollo 15 green and yellow glasses and revision of the volatile-assisted
750 fire-fountain theory, *Geochimica et Cosmochimica Acta*, 59(1), 201-215.

751 Gaddis, L., C. Rosanova, T. Hare, B. Hawke, C. Coombs, and M. Robinson (1998), Small lunar
752 pyroclastic deposits: a new global perspective, *LPI(1807)*, 1807.

753 Gaddis, L. R., B. R. Hawke, M. S. Robinson, and C. Coombs (2000), Compositional analyses of
754 small lunar pyroclastic deposits using Clementine multispectral data, *Journal of Geophysical*
755 *Research: Planets*, 105(E2), 4245-4262.

756 Gaddis, L. R., C. M. Pieters, and B. R. Hawke (1985), Remote sensing of lunar pyroclastic
757 mantling deposits, *Icarus*, 61(3), 461-489.

758 Gaddis, L. R., M. I. Staid, J. A. Tyburczy, B. R. Hawke, and N. E. Petro (2003), Compositional
759 analyses of lunar pyroclastic deposits, *Icarus*, 161(2), 262-280.

760 Gaetani, G. A., and T. L. Grove (1998), The influence of water on melting of mantle peridotite,
761 *Contributions to Mineralogy and Petrology*, 131(4), 323-346.

762 Greenwood, J. P., S. Itoh, N. Sakamoto, P. Warren, L. Taylor, and H. Yurimoto (2011),
763 Hydrogen isotope ratios in lunar rocks indicate delivery of cometary water to the Moon, *Nature*
764 *Geoscience*, 4(2), 79-82.

765 Gustafson, J. O., J. F. Bell, L. R. Gaddis, B. R. Hawke, and T. A. Giguere (2012),
766 Characterization of previously unidentified lunar pyroclastic deposits using Lunar
767 Reconnaissance Orbiter Camera data, *Journal of Geophysical Research: Planets*, 117(E12).

768 Hapke, B. W., R. M. Nelson, and W. D. Smythe (1993), The opposition effect of the moon: the
769 contribution of coherent backscatter, *Science*, 260(5107), 509-511.

770 Hauri, E. H., T. Weinreich, A. E. Saal, M. C. Rutherford, and J. A. Van Orman (2011), High pre-
771 eruptive water contents preserved in lunar melt inclusions, *Science*, 333(6039), 213-215.

772 Head, J. W. (1974), Lunar dark-mantle deposits-possible clues to the distribution of early mare
773 deposits, paper presented at Lunar and Planetary Science Conference Proceedings.

774 Head, J. W., and L. Wilson (2017), Generation, ascent and eruption of magma on the Moon:
775 New insights into source depths, magma supply, intrusions and effusive/explosive eruptions
776 (Part 2: Predicted emplacement processes and observations), *Icarus*, 283, 176-223.

777 Heiken, G., and D. McKay (1977), Model for eruption behavior of a volcanic vent in Eastern
778 Mare Serenitatis *Rep.*, Los Alamos Scientific Lab., NM (USA).

779 Heiken, G. H., D. T. Vaniman, and B. M. French (1991), Lunar sourcebook-A user's guide to the
780 moon, *Research supported by NASA.*, Cambridge, England, Cambridge University Press, 1991,
781 753 p. No individual items are abstracted in this volume.

782 Hess, P. C., and E. Parmentier (1995), A model for the thermal and chemical evolution of the
783 Moon's interior: Implications for the onset of mare volcanism, *Earth and Planetary Science*
784 *Letters*, 134(3-4), 501-514.

785 Hirth, G., and D. L. Kohlstedt (1996), Water in the oceanic upper mantle: implications for
786 rheology, melt extraction and the evolution of the lithosphere, *Earth and Planetary Science*
787 *Letters*, 144(1-2), 93-108.

788 Hui, H., Y. Guan, Y. Chen, A. H. Peslier, Y. Zhang, Y. Liu, R. L. Flemming, G. R. Rossman, J.
789 M. Eiler, and C. R. Neal (2017), A heterogeneous lunar interior for hydrogen isotopes as
790 revealed by the lunar highlands samples, *Earth and Planetary Science Letters*, 473, 14-23.

791 Krumbein, W. C. (1934), Size frequency distributions of sediments, *Journal of sedimentary*
792 *Research*, 4(2), 65-77.

793 Li, S., and R. E. Milliken (2016), An empirical thermal correction model for Moon Mineralogy
794 Mapper data constrained by laboratory spectra and Diviner temperatures, *Journal of Geophysical*
795 *Research: Planets*, 121(10), 2081-2107.

796 Li, S., and R. E. Milliken (2017), Water on the surface of the Moon as seen by the Moon
797 Mineralogy Mapper: Distribution, abundance, and origins, *Science advances*, 3(9), e1701471.

798 Lock, S. J., S. T. Stewart, M. I. Petaev, Z. Leinhardt, M. T. Mace, S. B. Jacobsen, and M. Cuk
799 (2018), The origin of the Moon within a terrestrial synestia, *Journal of Geophysical Research:*
800 *Planets*, 123(4), 910-951.

801 Longhi, J. (1992), Experimental petrology and petrogenesis of mare volcanics, *Geochimica et*
802 *Cosmochimica Acta*, 56(6), 2235-2251.

803 Longhi, J. (2006), Petrogenesis of picritic mare magmas: constraints on the extent of early lunar
804 differentiation, *Geochimica et Cosmochimica Acta*, 70(24), 5919-5934.

805 Lucey, P., R. Korotev, J. Gillis, L. Taylor, D. Lawrence, B. Campbell, R. Elphic, B. Feldman, L.
806 Hood, and D. Hunten (2006), New views of the moon, *Rev. Mineral. Geochem*, 83-219.

807 McCubbin, F. M., A. Steele, E. H. Hauri, H. Nekvasil, S. Yamashita, and R. J. Hemley (2010a),
808 Nominally hydrous magmatism on the Moon, *Proceedings of the National Academy of Sciences*,
809 107(25), 11223-11228.

810 McCubbin, F. M., A. Steele, H. Nekvasil, A. Schnieders, T. Rose, M. Fries, P. K. Carpenter, and
811 B. L. Jolliff (2010b), Detection of structurally bound hydroxyl in fluorapatite from Apollo Mare
812 basalt 15058, 128 using TOF-SIMS, *American Mineralogist*, 95(8-9), 1141-1150.

813 Milliken, R. E. (2006), *Estimating the water content of geologic materials using near-infrared*
814 *reflectance spectroscopy: Applications to laboratory and spacecraft data*.

815 Milliken, R. E., and S. Li (2017), Remote detection of widespread indigenous water in lunar
816 pyroclastic deposits, *Nature geoscience*, 10(8), 561-565.

817 Milliken, R. E., and J. F. Mustard (2005), Quantifying absolute water content of minerals using
818 near-infrared reflectance spectroscopy, *Journal of Geophysical Research: Planets*, 110(E12).

819 Milliken, R. E., and J. F. Mustard (2007a), Estimating the water content of hydrated minerals
820 using reflectance spectroscopy: I. Effects of darkening agents and low-albedo materials, *Icarus*,
821 189(2), 550-573.

822 Milliken, R. E., and J. F. Mustard (2007b), Estimating the water content of hydrated minerals
823 using reflectance spectroscopy: II. Effects of particle size, *Icarus*, 189(2), 574-588.

824 Mueller, S. B., B. F. Houghton, D. A. Swanson, M. Poret, and S. A. Fagents (2019), Total grain
825 size distribution of an intense Hawaiian fountaining event: case study of the 1959 Kīlauea Iki
826 eruption, *Bulletin of Volcanology*, 81(7), 43.

827 Rutherford, M. J., J. W. Head, A. E. Saal, E. Hauri, and L. Wilson (2017), Model for the origin,
828 ascent, and eruption of lunar picritic magmas, *American Mineralogist: Journal of Earth and*
829 *Planetary Materials*, 102(10), 2045-2053.

830 Saal, A. E., E. H. Hauri, M. L. Cascio, J. A. Van Orman, M. C. Rutherford, and R. F. Cooper
831 (2008), Volatile content of lunar volcanic glasses and the presence of water in the Moon's
832 interior, *Nature*, 454(7201), 192-195.

833 Saal, A. E., E. H. Hauri, J. A. Van Orman, and M. J. Rutherford (2013), Hydrogen isotopes in
834 lunar volcanic glasses and melt inclusions reveal a carbonaceous chondrite heritage, *Science*,
835 340(6138), 1317-1320.

836 Shearer, C., and J. Papike (1993), Basaltic magmatism on the Moon: A perspective from
837 volcanic picritic glass beads, *Geochimica et Cosmochimica Acta*, 57(19), 4785-4812.
838 Shearer, C. K., P. C. Hess, M. A. Wieczorek, M. E. Pritchard, E. M. Parmentier, L. E. Borg, J.
839 Longhi, L. T. Elkins-Tanton, C. R. Neal, and I. Antonenko (2006), Thermal and magmatic
840 evolution of the Moon, *Reviews in Mineralogy and Geochemistry*, 60(1), 365-518.
841 Watson, E., and J. Bender (1980), Diffusion of cesium, samarium, strontium, and chlorine in
842 molten silicate at high temperatures and pressures, paper presented at Geol. Soc. Am. Abstr.
843 Program.
844 Weitz, C. M., J. W. Head III, and C. M. Pieters (1998), Lunar regional dark mantle deposits:
845 Geologic, multispectral, and modeling studies, *Journal of Geophysical Research: Planets*,
846 103(E10), 22725-22759.
847 Wendlandt, R. F. (1991), Oxygen diffusion in basalt and andesite melts: experimental results and
848 discussion of chemical versus tracer diffusion, *Contributions to Mineralogy and Petrology*,
849 108(4), 463-471.
850 Wetzel, D. T., E. H. Hauri, A. E. Saal, and M. J. Rutherford (2015), Carbon content and
851 degassing history of the lunar volcanic glasses, *Nature Geoscience*, 8(10), 755-758.
852 Wetzel, D. T., M. J. Rutherford, S. D. Jacobsen, E. H. Hauri, and A. E. Saal (2013), Degassing of
853 reduced carbon from planetary basalts, *Proceedings of the National Academy of Sciences*,
854 110(20), 8010-8013.
855 Wieczorek, M. A., G. A. Neumann, F. Nimmo, W. S. Kiefer, G. J. Taylor, H. J. Melosh, R. J.
856 Phillips, S. C. Solomon, J. C. Andrews-Hanna, and S. W. Asmar (2013), The crust of the Moon
857 as seen by GRAIL, *Science*, 339(6120), 671-675.
858 Wilson, L. (1980), Relationships between pressure, volatile content and ejecta velocity in three
859 types of volcanic explosion, *Journal of Volcanology and Geothermal Research*, 8(2-4), 297-313.
860 Wilson, L., and J. Head III (2003), Deep generation of magmatic gas on the Moon and
861 implications for pyroclastic eruptions, *Geophysical Research Letters*, 30(12).
862 Wilson, L., and J. W. Head (2017), Generation, ascent and eruption of magma on the Moon:
863 New insights into source depths, magma supply, intrusions and effusive/explosive eruptions
864 (Part 1: Theory), *Icarus*, 283, 146-175.
865 Wilson, L., and K. Keil (2012), Volcanic activity on differentiated asteroids: A review and
866 analysis, *Geochemistry*, 72(4), 289-321.
867 Wilson, L., K. Keil, and T. J. McCOY (2010), Pyroclast loss or retention during explosive
868 volcanism on asteroids: Influence of asteroid size and gas content of melt, *Meteoritics &*
869 *Planetary Science*, 45(8), 1284-1301.
870 Zhang, Y., and E. M. Stolper (1991), Water diffusion in a basaltic melt, *Nature*, 351(6324), 306-
871 309.
872
873